Annals of Nuclear Energy 124 (2019) 472–489

Contents lists available at ScienceDirect

Annals of Nuclear Energy

journal homepage: www.elsevier.com/locate/anucene

CANDU-6 operation simulations using accident tolerant cladding candidates

A. Naceur *, G. Marleau

Institut de Génie Nucléaire, École Polytechnique de Montréal, P.O. Box 6079, Station Centre-Ville, Montréal, Québec H3C 3A7, Canada

ARTICLE INFO

Article history:
Received 8 May 2018
Received in revised form 11 September 2018
Accepted 11 October 2018
Available online 19 October 2018

Keywords:
CANDU-6
Accident tolerant claddings
Zicaloy-II
SiC
FeCrAl
APMT
304SS
310SS

ABSTRACT

The 3D DRAGON-DONJON capabilities are exploited to simulate CANDU-6 (Canada Deuterium Uranium) core follow-up with alternate cladding materials. Aluminium-based alloys (FeCrAl and APMT), nickel-based alloys (304SS and 310SS) and silicon carbide (SiC) are compared with Zircaloy-II. High thermal captures in aluminium and nickel-based systems imply ^{235}U enrichment, which results in a lower breeding ratio and a 1.1 ppm to a 1.4 ppm higher boron concentration than the current CANDU-6 reactor. Natural enrichment is preserved for SiC system, while providing a 3.4 mk increase in core reactivity with boron poisoning conditions similar to the reference CANDU bundle. The enriched systems' spectral hardenings result in a 246 kW lower channel power. Throughout the cycle, the new ATF operation compliances are compared to the CANDU-6 license limits. The liquid zone controllers and adjusters effects on power flattening are investigated. An 8-bundle shift on power refueling scheme based on the CANDU channel age model is implemented and tested. The cores' dynamic responses to a loss of regulation control event and to an instantaneous or gradual recovery of reactivity regulation devices are also studied. By uniformly perturbing the core global and bundle local parameters, new reactivity coefficients are determined and cores' responses are compared over a large spectrum of moderate and severe accident scenarios.

1. Introduction

In a typical CANDU-6 reactor, pin cladding is the first safety barrier for radionuclides retention, followed by the pressure tube, the calandria tube, the calandria vessel and finally the reactor containment building. The first 3 barriers use zirconium-based alloys. Zr-based fuel cladding originates from Admiral Hayman Rickover visit to the Clinton Engineer Works (Oak Ridge, TN) in June 1946 (Terrani, 2018), when he decided to use zirconium as fuel cladding in the PWR-S1W, the land-based prototype reactor for the U.S. Navy's Nautilus submarine (Rickover, 1975). The Rickover decision was then endorsed when Kaufmann (1948) at MIT and Pomerance (1948) at Oak Ridge succeeded in separating the highly absorbing hafnium impurity from a zirconium specimen. In Canada, unique technical challenges (Lewis, 1956) for the ZEEP (Zero Energy Experimental Pile) and NRX (National Research Experimental) facilities highlighted that significant changes had to be made to the structure materials to operate in high pressures and temperatures environment (Chaplin, 2014). Changing fuel cladding from aluminium to nickel and hafnium-free Zircaloy-II (Page, 1976), on the one hand, and adopting a zirconium-niobium alloy pressure tube rather than an aluminium pressure vessel design (Rae, 1997), on the other hand, are 2 of the 3 major changes introduced by AECL (Atomic Energy of Canada Limited) during the 22 MW NPD (Nuclear Power Demonstration) reactor design work in August 1955 (Hurst, 1997; Chaplin, 2014). Due to their sufficient neutron transparency (Pomerance, Oct 1952), excellent aqueous corrosion resistance (Goldman, 1953; Kass, 1954; Lustman and Kerze, 1955; Motta et al., 2015), high melting point (1852 °C), greatly improved mechanical strength (Ambartsumyan et al., 1959; IAEA, 1993), excellent weldability and impermeability to trapped fission gases (Merckx, 1958), zirconium-based alloys are now widely selected as structure materials for water-cooled power reactors.

During the late 1960's and early 1970's, reactor designers and regulators understanding of the nuclear power system integral behavior established the current safety framework for nuclear industry (Zinkle et al., 2014). Given a deterministic analytical approach, the emergency core cooling system (ECCS) was designed to respond to loss-of-coolant accident (LOCA) and reactivity insertion accident (RIA) (Cheng, 1980). This design basis (DB) accident stipulated that a peak cladding temperature (>1204.45 °C) must be avoided (zirconium rapid transient oxidation), a maximum cladding oxidation (> 0.17 times the original cladding thickness) must not be reached (excessive hydrogen accumulation) with a

* Corresponding author.
E-mail addresses: ahmed.naceur@polymtl.ca (A. Naceur), guy.marleau@polymtl.ca (G. Marleau).

https://doi.org/10.1016/j.anucene.2018.10.026
0306-4549/

coolable cladding geometry (U.S. Atomic Energy Commission, 1973; Johnston, 1977). Canadian work on hydrogen in zirconium dates from the Zr-2.5Nb pressure tube adoption during NPD design work (Sawatzky and Ells, 2000). Hydrogen diffusion in Zircaloy-II was investigated over the temperature range 260–560 °C (Sawatzky, 1960), while the axial hydrogen diffusivity in Zr-2.5Nb was investigated over the temperature range 200–700 °C (Sawatzky et al., 1982). Over the years, active plant safety systems have ensured fuel pin protection while tolerating a 1200 °C maximum cladding temperature for less than 400 s (Karoutas et al., 2018). The Three Mile Island Unit 2 partial meltdown, March, 28th 1979, demonstrated that a beyond design basis (BDB) accident, where a zirconium temperature above 1200 °C was reached for more than 400 s, could occur (Corey, 1979; Rogovin, 1980; Karoutas et al., 2018). Zinkle et al. (2014) report that: "*[this accident] induced two important shifts in reactor safety assessment and implementation approaches. The first was to augment the deterministic approach with probabilistic risk assessment (PRA) to better capture the complexities of system behavior. The second shift was to transition away from active safety systems towards passively safe reactor concepts. While the former was adopted more readily, the latter is just now being realized and only in certain parts of the world [...]*". The Fukushima Daiichi Units 1–3 station blackout (SBO), March, 11th 2011, demonstrated that the active cooling system could be lost for several days (IAEA, 2015). Rapid zirconium oxidation in a high-temperature steam environment, followed by hydrogen accumulation, release and detonation, showed that core physical and chemical degradation and finally core complete meltdown is a credible scenario (Burns et al., 2012; Nuclear Energy Agency, 2012). This BDB incident challenged the modeling assumptions used in the PRA approach to quantify operational risk (Zinkle et al., 2014). Accordingly, significant international efforts (Goldner, 2012; Sowder, 2012; Koo et al., 2014; Brachet et al., 2015) were immediately placed on enhancing the nuclear fuel pin behavior in high-pressure steam environment at temperatures above 1200 °C. The so-called accident tolerant fuel (ATF) concept aims to cover the entire DB and BDB accident spectrum by tolerating cladding cooling loss for a longer time, while improving, or at least maintaining, the core neutronic performance during nominal conditions (Ott et al., 2014). After reviewing a wide range of candidates, Pint et al. (2013, 2015) show that alumina, chromia and silica are three conventional classes of protective oxide films that offer more than one hundred times improvement in oxidation resistance in steam-H_2 environments above 1200 °C. Although zirconia (ZrO_2) has exceptional thermodynamic stability in steam, Steinbrück et al. (Oct 2011) thermo-gravimetric tests with AREVA (Duplex DX-D4,M5®), Westinghouse ZIRLOTM and Russian 110 alloy show a strong correlation between formed zirconia (ZrO_2) morphology and oxygen and hydrogen uptake, leading to an exponential oxidation with temperature increase and finally cladding embrittlement. In the case of chromium protective coating on Zr-based alloys surface, the most important challenge is that 25–40 tonnes of zirconium remain in the reactor core and a fraction of the internal region is exposed to severe oxidizing environment (Terrani, 2018). In this paper, we pursue our previous work (Naceur and Marleau, 2018) on ATF-cladded bundle for CANDU-6 by looking at core follow-up, adopting non-zirconium claddings based on alumina, chromia and silica protective solutions.

Terrani (2018) reports that several United-States and Japan R&D programs are actually considering the powder metallurgical FeCrAl (~20wt.%Cr – 5%Al) alloys as an ATF cladding technology (Rebak et al., 2017; Sakamoto et al., 2017). High temperature steam FeCrAl oxidation resistance relies on 2 (top and bottom) adherent slow-growing alumina protective scale (Al_2O_3). Seven hours of 1100 °C cladding exposition in (O_2, N_2, H_2O) environments showed that the oxide growth kinetics are water and hydrogen independent (Hellström et al., 2015). This two-layered scale protects the original metal surface up to 1475−1500°C in high-pressure superheated-steam conditions (Pint, 2017). The Kanthal alloy APMT (Advanced Powder Metallurgy Tube), with 1.6% more Cr and 0.1% less Al, show a similar slow-growing solid-alumina diffusion barrier (with no scale spallation) after 8 h' exposure at 1350 °C (Pint et al., 2013) and 4 h' exposure at 1475 °C in steam and dry air environments (Pint et al., 2015). Yttrium (Y) and/or Hafnium (Hf) additions are then essential for a better scale adhesion. Nuclear-grade SiC composites (Snead et al., 2017) are highly regarded as the ideal ATF cladding material (Terrani, 2018). Owing to its protective SiO_2 layer, these ceramics exhibit a minimal mass change, an exceptional oxidation resistance up to at least 1700 °C in high pressure steam (Terrani et al., 2014). The well-known problems of SiC aqueous hydrothermal corrosion and plausible microfracture propagation under normal operating conditions or after a core shutdown are now being tackled with an adherent coated SiC solution (Ang et al., 2017; Ishibashi et al., 2017) that may also serve as a radionuclide barrier. Conventional 304-type stainless steel (Brassfield et al., 1968) has a lower steam-cladding oxidation rate than Zircaloy under LOCA conditions but a higher degradation at 1200 °C (Ishida et al., 1986). The study of this sheath will be maintained for its historical irradiation performance in the early decades (George et al., 2015) and its high burnup capabilities (Uwaba et al., 2011). Increasing both chromium and nickel contents as for the austenitic type 310SS (25Cr-20Ni) forms a thin chromia (Cr_2O_3) protective scale after 48 h exposure at 1200 °C in steam conditions (Pint et al., 2013). This scale is thinner than the alumina one and less adherent due to its high thermal expansion factor (Wright and Barry Dooley, 2011).

What we propose here is to compare the current CANDU-6 core neutronic performance to aluminium (FeCrAl and APMT), nickel (304SS and 310SS) and silicon carbide (SiC)-cladded cores analyzing burnup calculations, fresh core poisoning requirements, power and flux distributions, on-power core refueling behavior, loss of regulation control events and core global and local parameters perturbations. In Section 2, we describe the nuclear database generation based on fuel lattice calculations and supercell simulations for reactivity devices and structures. We also present how the full-core will be modeled and the refueling scheme that will be considered. In Section 3, we analyze the core behavior under normal and accidental conditions. Finally, in Section 4 we draw conclusions and highlight future work.

2. Methodology

The CANDU-6 reactor is a cylindrical stainless steel vessel that lies horizontally and is filled with low temperature heavy water (D_2O) moderator, and 380 concentric horizontal (*Z*-axis) calandria and pressure tubes that contain fuel bundles. The moderator is kept essentially at atmospheric pressure, fulfills the reflector's role and is circulated through a purifier and a heat exchanger. The fuel channels are supported by the calandria end shields and are placed on a square lattice pitch of 28.575 cm. Each channel is filled with 12 identical fuel bundles 49.53 cm long. The inlet and outlet end shields are connected, through a piping system, to the D_2O coolant manifolds. The high pressure and temperature coolant flows in opposite directions in two adjacent pressure tubes in a checkerboard pattern (St-Aubin and Marleau, 2005). Reactivity measurements and control devices penetrate the calandria perpendicularly to the pressure tubes (*X* and *Y*-axis) and are located between channels rows and columns (see Fig. 1). This design facilitates secure fuel handling for on-line refueling. The on-power refueling system is designed to operate at all reactor power levels in order to compensate the daily reactivity loss (due

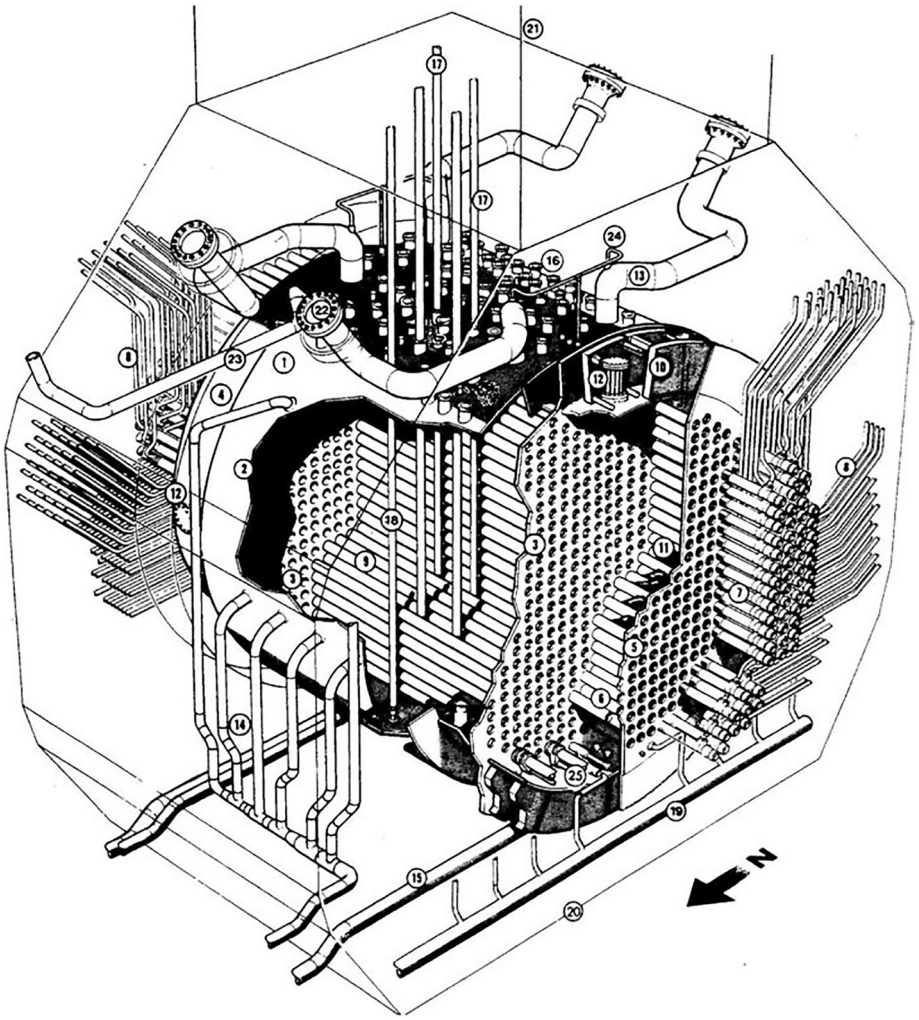

Fig. 1. CANDU reactor pressure vessel: *(1) calandria; (2) calandria main-shell; (3) calandria tubesheet; (4) calandria sub-shell; (5) fuelling tubesheet; (6) endshield lattice tube; (7) fuel channel end fittings; (8) feeders; (9) calandria tubes; (10) shield tank solid shielding; (11) endshield steel ball shielding; (12) manhole; (13) pressure relief pipes; (14) moderator inlet pipes; (15) moderator outlet pipes; (16) reactivity control unit nozzles; (17) shutoff unit thimble; (18) liquid zone control unit thimble; (19) shield cooling system piping; (20) shield tank; (21) shield tank extension; (22) rupture disc; (23) moderator overflow pipe; (24) pipe to moderator inlet header; (25) inlet outlet strainer.* (Luxat, 2009).

to fuel depletion). It can also be used to discharge a defective fuel bundle (Atomic Energy of Canada Limited, 2005). For safety analysis and fuel management purposes, the CANDU core modeling is a 3-level approach. The first level consists of computing the bare cell lattice properties to generate 2-group burnup dependent ($\mathcal{B}$) diffusion coefficients $D^g(\mathcal{B})$ and condensed and homogenized macroscopic cross sections $\Sigma^g(\mathcal{B})$, where g is the neutron energy group. WIMS (Donnelly, 1986) and DRAGON (Marleau et al., 1992), which are parts of the CANDU Industry Standard Tool-set (IST) of Codes for design and analysis (Rouben, 2002), can be used at this level. The second level aims to generate a 2-group condensed and homogenized incremental cross sections $\Delta\Sigma^g$ for all the reactivity devices that may be inserted in the reactor. This requires supercell calculations where reactivity devices are inserted vertically at the center of a lattice composed of two 3D horizontal fuel cells. All possible device configurations have to be considered (Roy et al., 1994). DRAGON is most often used for 3D CANDU supercell transport calculations (Garland, 2014). The final level is the reactor full-core modeling in 3D Cartesian geometry. Using the cross section libraries generated in the first two levels, the 2-group 3D diffusion equation is solved and core-wide flux distributions are then computed. There are several codes that have been validated against CANDU-6 operation data and can be used at this level, including RFSP (Carruthers and Chow, 1997; Shen and Schwanke, 2012), DONJON (Varin et al., 2004) and SORO (Shanes et al., 2006).

2.1. CANDU-6 cell review

Each cell of the lattice consists of a fuel bundle surrounded by two concentric pressure and calandria tubes. A cold low pressure D_2O moderator surrounds the calandria tube. An helium gas gap ensures insulation of the calandria tube from the hot D_2O coolant flowing in the pressure tube. A standard 37-element fuel bundle (1, 6, 12 and 18 UO_2 cladded pins per annular ring) is used and is illustrated in Fig. 2. The D_2O moderator and coolant purity are assumed to be, respectively, 99.92 at.% and 99.3 at.%. Table 1 lists, for the 6 claddings selected in this work (all 418μm thick), the material density (in g/cm^3), macroscopic thermal capture cross section (Σ_c) ratio against Zircaloy-II (Σ_{c-Zr}) and isotopic compositions (in weight percentage). The listed cross sections are group condensed using the flux obtained following a lattice calculations with an energy cut at 4 eV. In our study, the reference zirconium alloy (Zircaloy-II) is compared with silicon carbide (SiC), iron chromium aluminum alloy (FeCrAl), Kanthal advanced powder metallurgical (APMT), 304 and austenitic type 310 stainless steel (respectively 304SS and 310SS). These claddings were considered

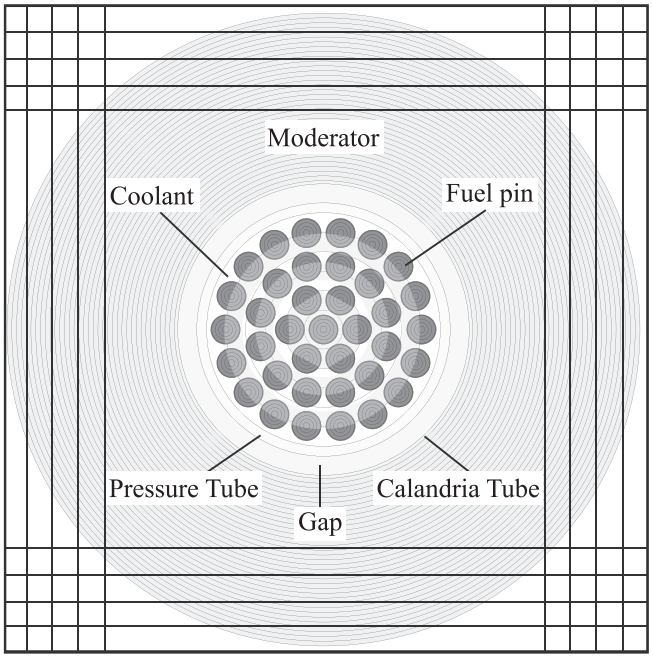

Fig. 2. CANDU 37-element bundle cell.

because of their high temperature steam oxidation resistance (Pint et al., 2013; Pint et al., 2015) and significantly lower specimen mass change than Zircaloy (Ott et al., 2014).

Our first computation scheme is based on the lattice and supercell code DRAGON5 (Marleau et al., 2018). The 2D cell calculations are first performed using a 172-groups JEFF-3.1 WIMSD-4 library (Koning et al., 2006). The generalized Stamm'ler self-shielding approach (Hébert and Marleau, 1991) is applied to update the resonant isotopes microscopic cross sections. Using tracking and cross section information, the scattering-reduced collision probabilities are computed. The multigroup transport equation is solved using a B1 homogeneous leakage model and constant power fuel depletion of 31.9713 kW/kg is assumed. Cross sections are homogenized over the complete cell and condensed to 2 energy groups. ^{135}Xe production rate is followed and extracted during the complete burnup cycle. At each depletion step, all nuclear data are recovered and tabulated in a database as a function of global and local parameters (representing normal and accidental conditions). Global parameters (e.g. moderator purity, density or poison load) are CANDU lattice characteristics, while local parameters (e.g. temperatures, coolant density or neutron exposure rate) are homogenized bundle mixture characteristics (Marleau et al., 2018).

The same ^{235}U enrichment criteria suggested in the previous paper (Naceur and Marleau, 2018) for different claddings is considered in this study. Enrichment is increased in such a way that the bundle effective neutron multiplication factor ($\bar{k}_{\text{eff}}$) averaged over the complete cycle (300 days) is the same as the effective reference [UO_2, Zr]. 300 days is the fuel bundle average residence time in CANDU reactors. Table 2 summarizes the converged results when the criticality criterion is satisfied for all cells. (e_{nat_U}) is the natural uranium enrichment, while (e_{enr_U}) is the optimized fuel enrichment.

2.2. CANDU-6 supercell model

CANDU reactivity devices are associated either with the reactor regulating system (RRS) or the emergency shutdown system (ESS). There are 3 types of RRS devices: 6 liquid zone controllers (LZC), each containing 2 or 3 compartments half-filled with demineralized H_2O, that provide the primary means for continuous power modulation in 14 zones of the core; 21 stainless steel adjuster rods (ADJ), grouped in 7 banks, that are normally inserted in the core to flatten the flux distribution; 4 mechanical control absorbers (MCA) normally withdrawn that can be dropped by gravity or with controlled speed to cause a quick power reduction or to deal with transient conditions. There are also 3 types of ESS devices: 28 shutoff rods (SOR), held above the core, that respond automatically to any failure or RRS loss by making the reactor highly subcritical while maintaining cooling capabilities; 6 gadolinium nitrate poisoning nozzles (GPN), passing horizontally through the core, that act as a redundant ESS making immediate recovery impossible; boron poisoning nozzles (BPN) to control fresh fuel excess reactivity (St-Aubin and Marleau, 2015). Both RRS and SOR devices are vertical (*Y*-axis), while GPN and BPN are horizontal (*X*-axis). Thus, an appropriate 3D transport calculation is needed to model these devices. The 3D supercell model consists of two horizontal fuel bundles that surround the reactivity device in a 3D Cartesian mesh, as depicted in Fig. 3.

The 3D transport equation is solved using the collision probability method (CP) with the device in the inserted (*in*) and extracted (*out*) positions. Homogenization is performed over the complete supercell volume. For each reaction of type *x*, 2-group condensed and homogenized incremental cross sections $\Delta\Sigma_x^g = \Sigma_x^{g,in} - \Sigma_x^{g,out}$ and diffusion coefficients ΔD^g are computed and stored in a second database. The same properties are generated for all CANDU reactivity and structure materials present under normal operating conditions. For the LZC, 2 successive 3D transport computations are also required corresponding to the case when compartments are, respectively, filled with air and light water (H_2O) (St-Aubin and Marleau, 2015b). The devices and structures considered are:

- LZC, ADJ, MCA, SOR, GPN, BPN, VFD (vertical flux detectors) and HFD (horizontal flux detectors) brackets and locators;
- ADJ, MCA, SOR, GPN, BPN, VFD and HFD Zircaloy guide tubes;
- LZC, ADJ, MCA and SOR coupling nuts and tensioning springs;
- ADJ supporting bars and cables;
- 8 moderator injectors.

2.3. CANDU-6 full core model

A 3D Cartesian mesh is used to represent the reactor 4560 fuel bundles, the D_2O radial reflector, the reactivity control devices and the reactor pressure vessel. Fig. 4 illustrates the central axial cut of a CANDU-6. The minimal discretization uses only one region (*kj*)

Table 1
Candidate cladding material properties.

Material	ρ_v [g/cm^3]	Σ_c/Σ_{c-Zr}	^{56}Fe	^{58}Ni	^{52}Cr	^{nat}B	^{91}Zr	^{28}Si	^{12}C	^{27}Al	^{59}Ni	^{55}Mn	^{96}Mo	^{179}Hf
Zircaloy-II	6.44	1.000	0.16	0.06	0.11	0.00031	99.71	–	–	–	–	–	–	–
SiC	2.58	0.663	–	–	–	–	–	70.08	29.92	–	–	–	–	–
FeCrAl	7.10	1.956	75.0	–	20.0	–	–	–	–	5.0	–	–	–	–
APMT	7.30	1.996	69.79	–	21.60	–	0.10	0.53	–	4.9	–	–	2.92	0.16
304SS	7.90	2.408	71.35	–	18.9	–	–	0.42	–	–	8.35	0.70	0.27	–
310SS	8.03	2.735	52.55	–	25.22	–	–	0.7	–	–	19.51	1.9	0.122	–

Table 2
Cycle converged mean multiplication factor.

	Zr	SiC	FeCrAl	APMT	304SS	310SS
$\bar{k}_{\text{eff}}(e_{\text{natU}})$	1.026239	1.029790	0.922744	0.919418	0.899505	0.884282
e_{enrU} [%]	0.711400	0.711400	1.049840	1.061905	1.132900	1.192371
$\bar{k}_{\text{eff}}(e_{\text{enrU}})$	1.026239	1.029790	1.026239	1.026239	1.026239	1.026239

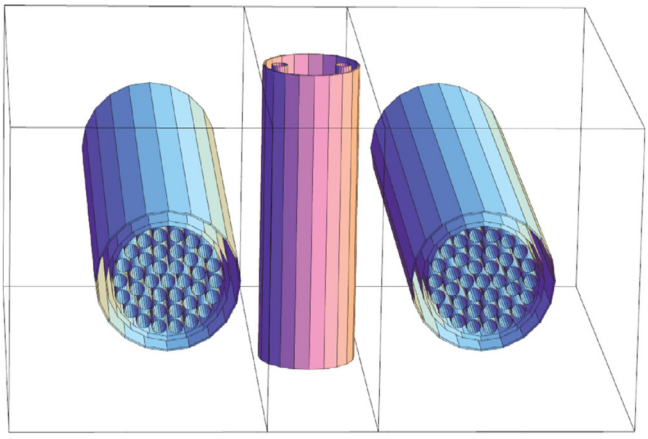

Fig. 3. CANDU supercell model for reactivity devices.

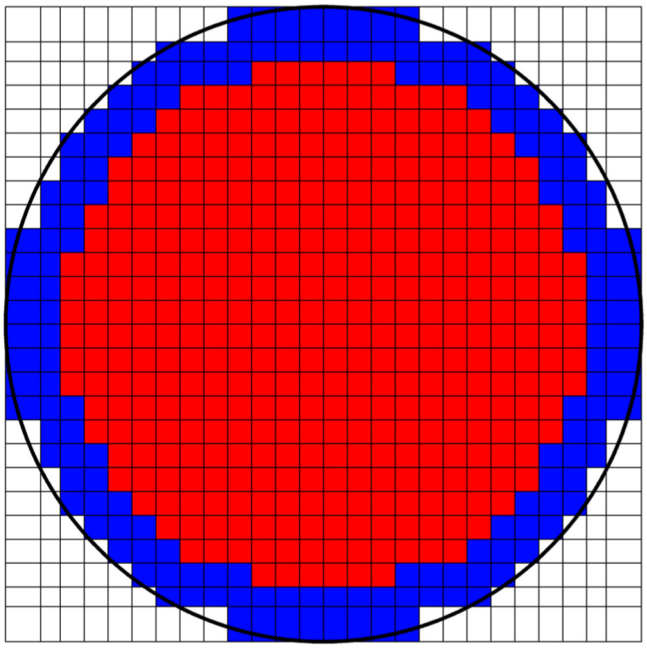

Fig. 4. CANDU reactor mesh along *xy* plans. *Red: fuel regions; Blue: reflector; Black line: calandria boundary; White: regions outside the core* (St-Aubin, 2013). (For interpretation of the references to colour in this figure legend, the reader is referred to the web version of this article.)

per fuel bundle (bundle k of channel j), which lead to 12 planes all 49.53 cm thick along the Z-axis. A finer mesh subdivision is introduced along the X and Y-axis to match the reactivity device limits. The exact configuration of the 380 channels is respected, as well as possible when approaching the cylindrical boundary, by using regions of varying heights and widths for the reflector. Some fictitious volumes are then added to complete a 3D rectangular prism with 8112 regions (St-Aubin, 2013). Regions crossing the calandria boundary see a zero incoming flux boundary condition. All fuel channels are grouped into 3 combustion zones (low, medium and high). The original fuel map is then modified by superimposing the reactivity mechanisms and the structural materials. RRS and ESS devices are introduced independently as 3D boxes of width 28.575 cm (in x) by 49.53 cm (in z) and of varying heights (in y) (St-Aubin, 2013). Here, all devices have time-dependent displacements and can be used in transient simulations. For regulating purposes, ADJ can be inserted or extracted, individually or per group, at constant or variable speeds. LZC water filling level and rate can also be controlled at every moment in each one of the 14 control zones (Hébert et al., 2018). The device position (y) is then recomputed. Day-by-day, the instantaneous fuel bundle burnup ($\mathcal{B}_{kj}$) is computed and the core nuclear data are updated using the reactivity devices actual positions as: $\Sigma^g_{x,kj} = \Sigma^g_x(\mathcal{B}_{kj}) + \Delta\Sigma^g_{x,kj}(y)$. Fig. 5 depicts the configuration of the reactivity devices in the xz-plane.

Our third step is based on the 3D full-core simulation code DONJON5 (Hébert et al., 2018). DONJON5 is designed around advanced discretization algorithms and iteration strategies programmed in the TRIVAC multigroup diffusion solver (Hébert, 1987). Once the fuel (burnup-dependent), reflector, reactivity devices and structure materials databases are available, the CANDU-6 core follow-up can be considered. CANDU-6 geometry is first constructed plane-by-plane, each mesh region being linked to a specific material mixture. 3D tracking is then performed using a mesh centered finite difference approximation. Devices, structure materials and detectors are then superimposed on the fuel lattice. ADJ (and LZC) are immediately grouped into specific banks (and zones) for regulating purpose. An instantaneous burnup model is

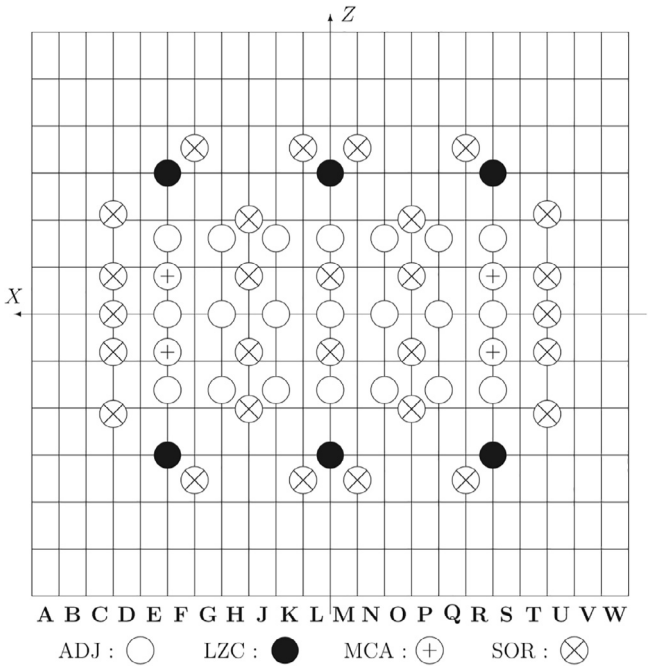

Fig. 5. CANDU reactivity device configurations in the xz-plane (St-Aubin and Marleau, 2015).

selected with the specified core global parameters and bundles local parameters and the fuel map object is constructed. Although the on-power refueling requires information about the bundle exact position, some core regions may contain mixed fuel and reflector parts. The fuel map allows us to associate fine geometric resolution and bundles definition (functions of power and burnup) (Varin et al., 2004). Two macroscopic libraries are first generated where the reflector properties are first built from the multi-parameter DRAGON database and bundle nuclear properties are computed with local parameter interpolations. A third macroscopic library is generated after interpolation of reactivity devices and structure materials databases. A complete library is finally built containing every material region properties, over the whole mesh-split core geometry. TRIVAC modules (Hébert, 2017) are sequentially called to compute the finite element system matrices and solve the eigenvalue problem. Fluxes are converged with a relative precision of 10^{-6}. Fuel bundle average fission power is fixed at 615 kW, typical of the CANDU-6 producing 2061.4 MWth. A typical burn step of 2 full-power days (FPD) is selected during the cycle.

2.4. Core refueling sequence

For operating CANDU reactors, the list of channels to be refueled is generally based on the core actual history tracking, the on-line flux mapping system, the in-core detector readings, the LZC water fills (Rouben, 1997) and the bundle history effect (Varin and Marleau, 2006). Several criteria, which are often difficult to satisfy at the same time, must be prioritized by the reactor operator. An engineering judgment is then needed. Rouben (2014) shows that a good combination of channels due to be refueled will typically contain:

1. channels for which the time since the last refueling has almost reached the channel dwell time;
2. channels containing bundles with a high current burnup;
3. channels with low power and/or being in a low power zone;
4. channels which, selected together, ensure an instantaneous power distribution similar to the reference power shape and preserve axial, radial and azimuthal flux and power symmetry;
5. channels being mutually widely/reasonably separated to avoid power peaks and hot spots;
6. channels which will leave the LZC filling level in an acceptable range [20%, 70%]; and
7. channels which, taken together, provide exactly the balance needed to compensate the daily reactivity loss (i.e. which tend to leave the RRS is the desired operational range and positions).

This said, even if the inner core regions have the highest burnup levels, only some of the channels in these regions will be refueled. Secondly, not all the channels at the same radial position can be refueled simultaneously; a burnup distribution is required. Thirdly, close-neighbor channels are not to be refueled very closely in time. One method that was suggested by Rozon and Shen (2001) and recommended by Rouben (2014) is to define an *intelligent pattern* based on the CANDU channel age model (Wight and Sibley, 1977; Rouben, 1995). The channel age is the channel instantaneous fraction of its cycle irradiation since the last refueling; it can be used to define a particular refueling history. The first step is to implement the channel refueling order pattern in a very small core region (e.g. 6-channels-by-6-channels). The second step is to subdivide the CANDU core into 6×6 blocks and to start selecting channels intelligently in a sequential way by browsing all regions. The condition is that "*[...] whenever revisiting each* 6×6 *region the order within the region follows the pattern defined for the* 6×6 *square*" (Rouben, 2014). The core refueling sequence obtained is presented in Fig. 6.

3. Results

3.1. Fresh fuel k_{eff} depletion results

During normal operation of a CANDU reactor, LZC compartments are half filled, ADJ are fully inserted in the core, MCA and ESS devices are withdrawn. Fig. 7 shows the core effective multiplication factor (k_{eff}) evolution during the first operation cycle (initially contains only fresh fuel). Fig. 8 depicts the difference in the core k_{eff} between the alternate cladding material and Zircaloy-II. Table 3 lists the core excess in reactivity $\rho = (k_{\text{eff}} - 1)/k_{\text{eff}}$ at some selected times in full-power days (FPD). At the beginning of the

	1	2	3	4	5	6	7	8	9	10	11	12	13	14	15	16	17	18	19	20	21	22
A									358	91	39	67	162	234								
B						315	113	294	196	248	366	309	109	287	191	245	363					
C					59	33	208	346	19	219	61	25	202	340	14	213	55	31				
D				271	322	123	261	103	156	273	323	118	254	97	149	265	318	122	260			
E			333	7	184	51	377	135	334	8	185	44	371	172	327	1	179	50	376	133		
F			176	145	283	226	301	79	173	142	279	232	307	86	177	147	285	228	303	81		
G		241	360	93	40	69	164	236	353	88	37	76	171	243	361	95	42	71	166	238	355	
H		296	198	250	267	311	110	289	193	246	364	316	116	298	200	252	369	313	112	291	195	
J	210	348	21	221	63	27	204	342	16	215	57	35	211	350	23	223	65	29	206	344	18	217
K	262	105	158	275	324	119	256	99	151	267	319	125	263	107	160	276	325	121	258	101	153	269
L	278	137	336	10	187	46	372	129	329	3	181	53	379	139	338	12	189	48	374	131	331	5
M	292	72	167	132	270	224	299	77	172	140	277	216	290	70	165	130	268	222	297	75	170	138
N	154	229	345	82	30	66	161	233	351	87	36	58	152	227	343	80	28	64	159	231	349	85
O	102	281	183	239	356	308	108	286	190	244	362	302	100	280	182	237	354	306	106	284	188	242
P		332	6	207	49	24	201	339	13	212	54	17	194	330	4	205	47	22	199	337	11	
Q		90	144	259	314	117	253	96	148	264	317	111	247	89	143	257	312	115	251	94	146	
R			321	375	175	43	370	126	326	380	178	38	365	120	320	373	174	41	368	124		
S			168	134	272	214	288	68	163	128	266	220	295	74	169	136	274	218	293	73		
T				83	32	56	150	225	341	78	26	62	157	230	347	84	34	60	155			
U					357	300	98	278	180	235	352	305	104	282	186	240	359	304				
V						15	192	328	2	203	45	20	197	335	9	209	52					
W									141	255	310	114	249	92								

Fig. 6. Core refueling sequence selected.

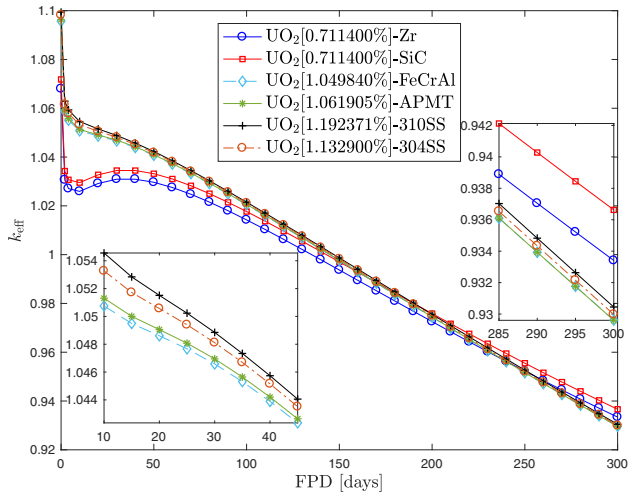

Fig. 7. Effective multiplication factor vs. core full-power days for various cladding candidates.

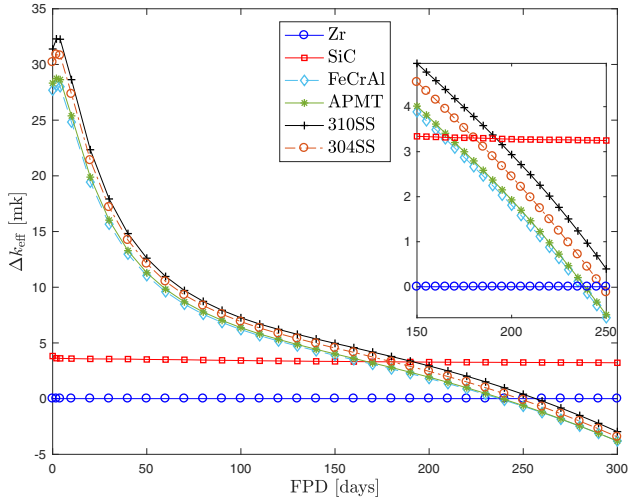

Fig. 8. Δk_{eff} from Zircaloy-II vs. core full-power days for various cladding candidates.

cycle (BOC), a large reactivity difference ($\Delta\rho$) is found between the cores with bundles cladded with Class I materials (Zr, SiC) and those with Class II materials (FeCrAl, APMT, 304SS and 310SS). Because ^{235}U is the only fissile nuclei present in freshly fueled CANDU's bundles, the core excess reactivity reflects exactly the bundles' enrichment level (Table 2), which in turn reflects the claddings' thermal neutron capture probabilities (Table 1). While the initial average reactivity difference ($\overline{\Delta}\rho$) between Class II systems and Zircaloy is of the order of 25.1 mk at BOC, it is reduced to 4.4 mk at middle of the cycle (MOC) and is negative (−4.1 mk) at the end of a cycle (EOC). For Class I materials, the core reactivity decreases rapidly until 10 FPD, then starts increasing until it reaches a maximum between 35 and 40 FPD, known as the plutonium peak. ^{239}Pu increases the core reactivity as it is produced. The observed time lag is due to some accumulation effect following the 2.4-days half-life of ^{239}Np the immediate ^{239}Pu parent (Garland, 2014). ^{239}Pu peak is 3.34 mk higher in SiC cladded core, which decreases the fuel delayed neutron fraction. A faster acting regulation system than for Zircaloy should be introduced. The core power may be reduced further until ^{239}Pu level is stable (Woddi et al., 2009). For Class II materials, no ^{239}Pu peak is observed.

This is due to the fact that the ^{238}U radiative captures (original ^{239}Pu parent) are 100 times less likely to occur than ^{235}U thermal absorptions. As a result, aluminium and nickel-cladded bundles will have a higher probability of fissile nuclei consumption than fissile nuclei production. Captures in fertile nuclei cannot balance ^{235}U burnup. After 50 FPD, all core reactivities decrease monotonically as irradiation progresses. ^{235}U is continuously consumed and the ^{239}Pu can no longer compensate the negative reactivity load resulting from the increasing fission products. This behavior can be confirmed by the bundle thermal-group fission yield cross section ($\nu\Sigma_f^2$) shown in Fig. 9 (*left*) and the bundle thermal group absorption cross section (Σ_a^2) shown in Fig. 9 (*right*).

It is also observed in Fig. 8 that nickel (or aluminium)-cladded cores are more supercritical than the silicon carbide cladded one up to the 190th day (165th day) and continue to dominate the CANDU reference core until the 250th day (235th day). Reaching these burnup levels, the ^{235}U fission rate can no longer compensate the cladding neutronic penalties. Using the less absorbing SiC cladding permits CANDU operation with natural uranium and produces at least 3.39 mk higher $\overline{\Delta}k_{\text{eff}}$ than Zircaloy-II.

3.2. Required poison concentration

The different fresh fuel excess reactivities presented in Table 3 must be compensated in a controlled manner. Natural Boron (20% ^{10}B) is added to the moderator to control the reactor BOC reactivity worth. Several iterations were needed in DRAGON-DONJON calculations chain to achieve criticality in diffusion results. A convergence criterion of 0.01 mk is selected for each system investigated. Table 4 presents the required boron concentration when the core criticality is reached. When the fuel is more enriched, the initial moderator system is more poisoned. Only 0.1 ppm larger boron concentration than the actual CANDU-6 conditions is needed for the silicon carbide system. For aluminium and nickel-cladded cores, the increase in boron concentration is from 11 to 13 times higher (still considerably lower than for PWR). Contrarily to what the insertion (or removal) of an RRS device shows, it was verified that no distortion in the flux distribution is observed. This observation is mainly due to the solubility of the introduced boron. The boron reactivity effect is then homogeneously distributed in the calandria.

As the excess reactivity gradually drops, boron concentration decreases. The ion exchanger resin removal rate should be tested with the new fuels. One way to make sure that the boron concentration is exactly the required concentration is to ensure that LZCs filling levels remain in an acceptable range (Bieman and Bird, 1992).

Table 3
Core excess reactivity at some selected periods.

	Zr	SiC	FeCrAl	APMT	304SS	310SS
ρ (0 FPD) [mk]	+63.7	+67.0	+87.3	+87.9	+89.4	+90.4
ρ (135 FPD) [mk]	+0.03	+3.37	+4.51	+4.65	+5.56	+5.18
ρ (150 FPD) [mk]	−6.34	−2.97	−2.42	−2.29	−1.76	−1.34
ρ (300 FPD) [mk]	−71.3	−67.7	−75.7	−75.7	−75.3	−74.8

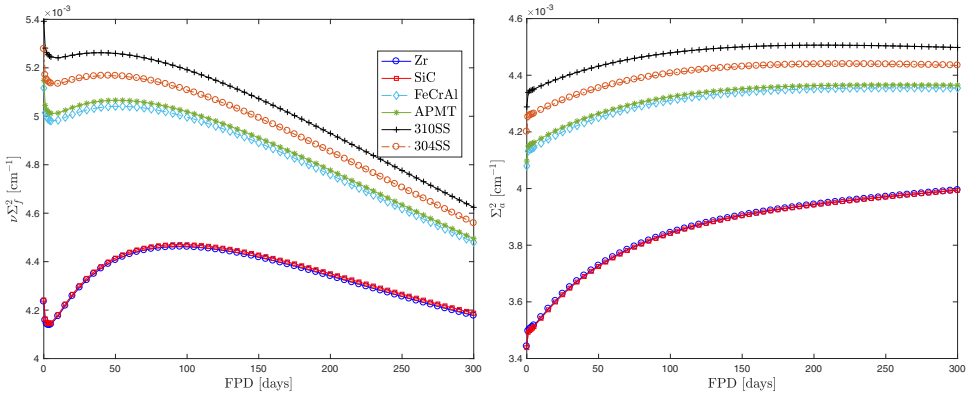

Fig. 9. Thermal-group fission yield cross section (*left*) and thermal-group absorption cross section (*right*).

Table 4
Required boron concentration at BOC.

	Zr	SiC	FeCrAl	APMT	304SS	310SS
k_{eff} ($[B^{10}] = 0$)	1.06800	1.07182	1.09569 92	1.09633	1.09820	1.09939
Boron $[B^{10}]$ (ppm)	1.63663	1.73085	2.78023	2.81207	2.94408	3.04740
Boron $[B^{10}]$ ($\times 10^{16}$ at/cm^3)	9.87686	10.44544	16.77831	16.97051	17.76716	18.39070
k_{eff} ($[B^{10}] \neq 0$)	1.00000	1.00001	1.00000	1.00000	1.00000	1.00000

3.3. Power profiles

Energy conversion factors (MeV/MJ) and the recoverable energy from neutron-induced reactions (also known as H-factors) (Hébert, 2016) are used to compute the bundle powers that are normalized in such a way that the overall reactor power is 2061.4 MWth. At every time steps, previous bundle burnups and powers are recovered to compute the new core's flux and power distributions. Fig. 10 shows the maximum channel and bundle powers generated during the complete cycle. Fig. 11 depicts the channel power profile as a function of the horizontal radial distance (in terms of fuel channel positions) at 35 FPD and 100 FPD for some selected rows (see Fig. 6 for row and column identification). Fig. 12 illustrates, for plane $z = 6$ at 35 FPD, the bundle power distribution as a function of the horizontal radial distance x and the vertical inter-bundles distance y (both in terms of fuel bundle positions).

The power radial and axial profiles show that all systems respond in a similar way to the CANDU known distributions (Rouben, 1997; Garland, 2014). The channels (and the bundles) with the highest powers are exactly in the same locations for all the cores under study. The radial (and axial) power increases towards the center of the core and decreases as one approaches the core periphery. The fuel is fresh so all cores show a higher fission rate in the core center and therefore the core internal regions burn at a higher rate. The different power depressions are mainly governed by the reactivity devices. For a uniformly fueled reactor without reactivity control devices, the radial flux distribution is the Bessel J_0 function, while the axial flux distribution corresponds to a cosine shape. Thus, power quickly decreases from the core center. Consequently, a high-localized bundle or channel power, exceeding the plant's operating license limits, may appear (Glasstone and Sesonske, 2012; Rouben, 2014). Control rods flatten and redistribute the power so that more channels (radially) and bundles (axially) contribute significantly to power. The overall global power remains constant while the local power limits are respected (Rouben, 2014). From Fig. 11 and Fig. 12, *left*, we conclude that the degree of radial flattening is satisfactory for all systems (maximum difference of 11 W in channel power reduction between Class-I and II materials). As one moves away from the reflector, a power gap is formed between cores cladded with Class I materials and those with Class II materials. Channel (or bundle) powers can be 245.8 kW (53.8 kW) higher in Zr and SiC sheathed

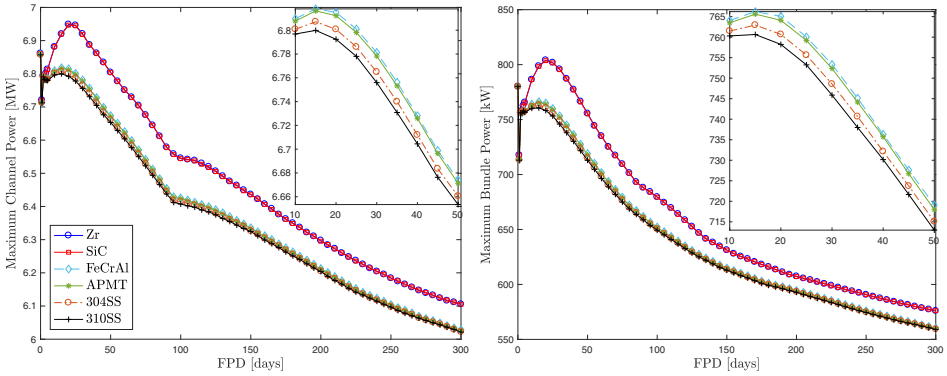

Fig. 10. Maximum channel powers (*left*) and maximum bundle powers (*right*) vs. core full-power days.

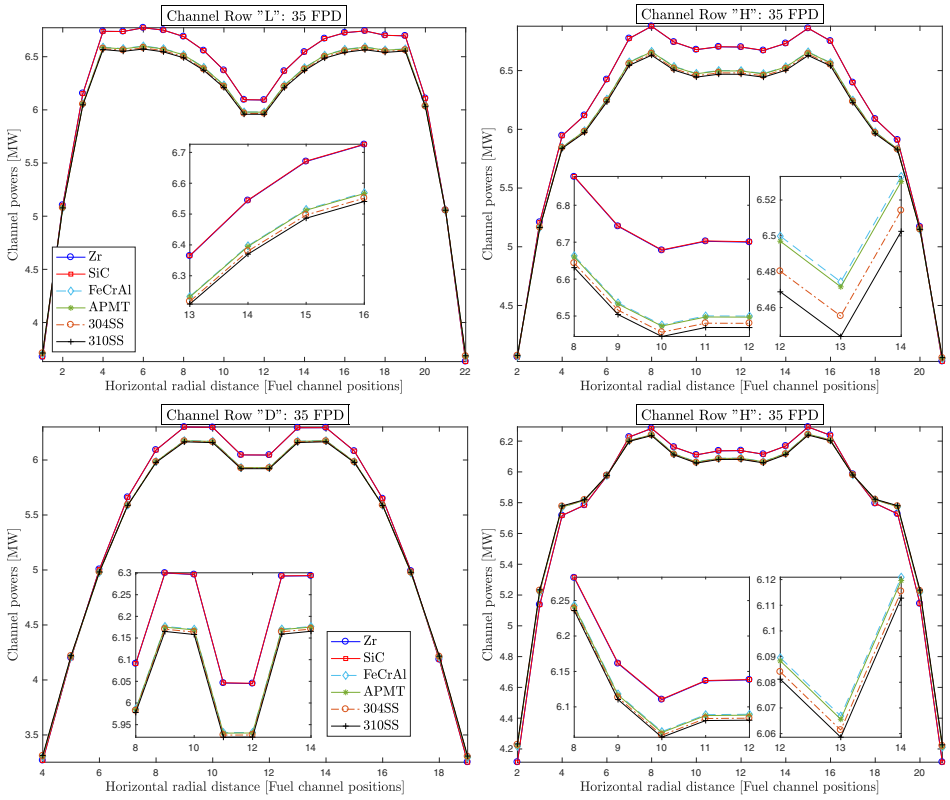

Fig. 11. Radial channel power distribution.

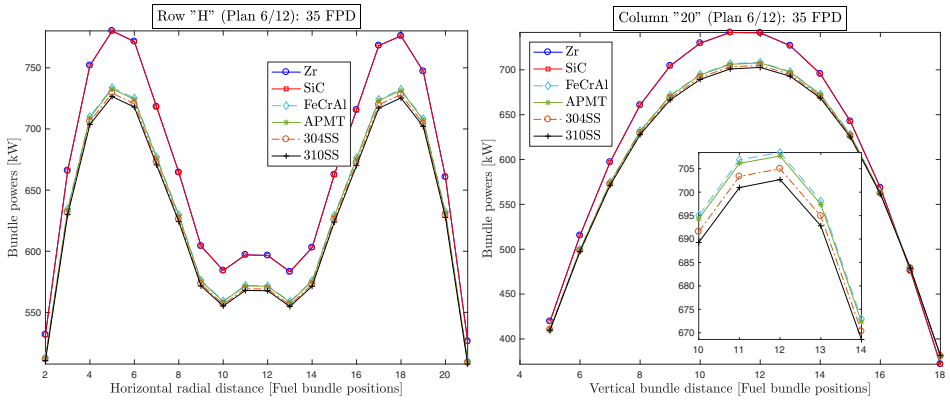

Fig. 12. Bundle power distribution at 35 FPD for plane $z = 6$ as a function of horizontal distance x in row "H" (*left*) and vertical distance y in column "20" (*right*).

cores than in aluminium and nickel-sheathed cores. Although ^{235}U enrichment levels (Table 2) and fission rates (Fig. 9, *left*) are higher in 310SS and 304SS cladded cores, local powers are found to be lower when compared to APMT and FeCrAl systems. This is mainly due to a spectrum hardening effect, as discussed in Section 3.4. At the ^{239}Pu peak (35–40 FPD), Zircaloy maximum channel (or bundle) power exceeds the silicon carbide system only by 1.45 kW (0.316 kW). SiC and Zr systems adopt the same power distributions because their flux distributions and fission yields are almost identical. Fig. 10 shows that operations are in compliance with the licensed maximum bundle and channel power which are respectively 935 kW and 7.3 MW for a CANDU-6 using the 37-element fuel bundle (D'Antonio and Donnelly, 1997). The time-averaged maximum channel and bundle power differences between the reference system and nickel-cladded (304SS and 310SS) systems are respectively 106.4 kW and 22.6 kW. These differences are reduced to 95.5 kW and 20.3 kW when the reference system is compared to the aluminium-based (FeCrAl and APMT) cores.

3.4. Thermal flux distribution

Fig. 13, Fig. 14 and Fig. 15 compare the thermal flux distribution between Class I and Class II-cladded cores at BOC, at 35 FPD (plutonium peak for Class I claddings) and just before refueling starts (100 FPD), respectively. Flux distribution differences between Zircaloy and silicon carbide-cladded systems are below 0.3%, while they are less than 4.5% between aluminium and nickel-cladded cores. Such differences cannot be visually ascertained. For this reason, only one distribution per cladding Class is presented at each figure. The height of 598.305 cm represents the reactor's upper periphery. The other two heights, 152.535 cm and 276.360 cm, respectively illustrate the systems' responses in the presence of 7

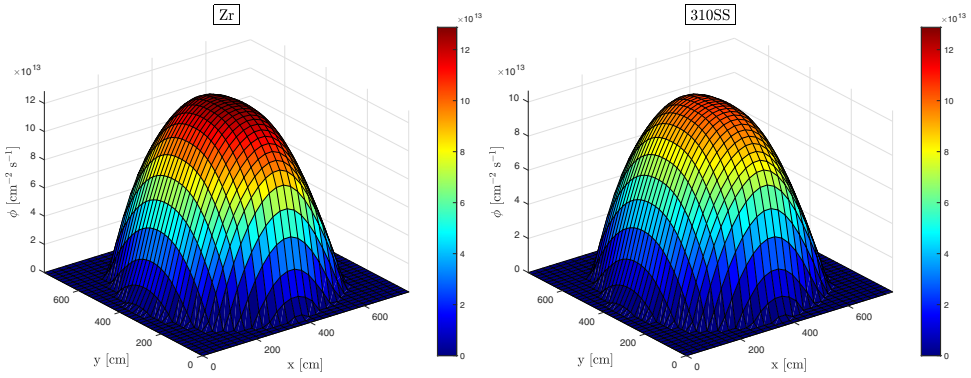

Fig. 13. Thermal flux distribution at BOC at 598.305 cm height.

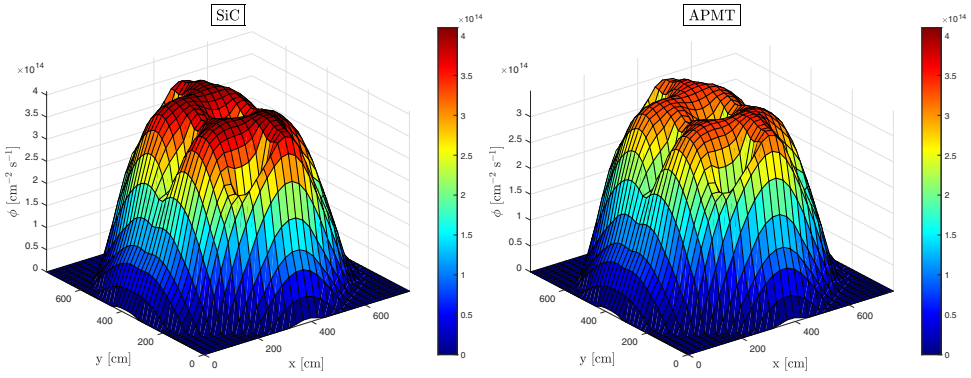

Fig. 14. Thermal flux distribution at 35 FPD at 152.535 cm height.

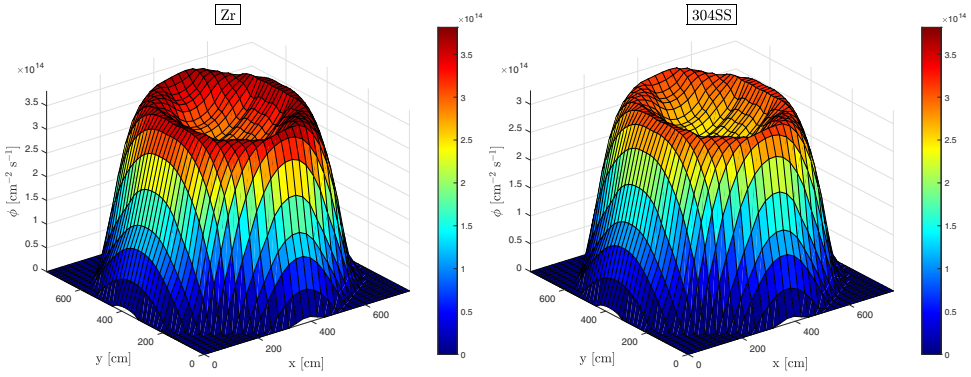

Fig. 15. Thermal flux distribution at 100 FPD at 276.360 cm height.

half-filled LZC devices and 2 fully inserted ADJ banks. Fig. 13–15 show that the flux distribution symmetry is preserved. Figs. 14 and 15 show, that regardless of the inserted device type (LZC or ADJ) or number, the degree of radial flux flattening remains the same for all claddings. At each time step, the core hottest and coldest points are found at exactly the same place in every system investigated. At 35 FPD, the thermal neutron flux at the core hottest point is found to be respectively 19.81% and 18.31% lower in the 310SS and 304SS-cladded cores than in the CANDU reference system. These differences are reduced to 16.52% and 16.06% when compared to the APMT and FeCrAl-cladded cores. Changes in the thermal flux are only 0.26% when the Zircaloy system is compared with the silicon carbide one. These flux differences remain very similar throughout the cycle in the inner and the outer reactor regions. The aluminium and nickel-cladded cores' thermal flux deviate from the CANDU known distribution toward the high energy region because thermal absorption cross sections are larger. The cladding with the highest radiative capture rate (Table 1) is the most absorbent bundle in the thermal group (Fig. 9, *right*). The same cladding induces the most important spectrum hardening effect (Fig. 13 and Fig. 15). A higher spectrum hardening is seen for the bundle and channel with lowest power (Fig. 11 and Fig. 12).

This is expected for thermal neutron reactors where the power distribution within the core is:

$$P(\vec{r}) = \kappa \sum_g \Sigma_f^g(\vec{r}) \phi^g(\vec{r}) \tag{1}$$

with $\vec{r}$ the bundle spatial coordinates and κ (about 200 MeV) the energy released per fission.

An increase in reactivity is observed in Class II systems (Fig. 7 and Table 3) as a result of the ^{235}U enrichment, which gives a higher fission to absorption ratio

$$R_{f/a} = \frac{\int \nu\Sigma_f(E)\phi(E)\mathrm{d}E}{\int \Sigma_a(E)\phi(E)\mathrm{d}E} \quad (2)$$

without necessarily having a higher flux distribution. Class II neutronic penalties harden the flux spectrum which results in a lower ^{239}Pu production rate and a lower ^{239}Pu resonance contribution (0.295 eV). Despite the higher initial criticality, the system reactivity is more quickly reduced (Fig. 7) and the local bundle powers and burnups are lower (Fig. 12).

3.5. Core refueling

Fueling machine maintenance and operating costs are minimized when the channel-visit rate is reduced. Increasing the number of bundles loaded per channel visit is then desirable. It is also not possible for a refueling machine to maintain, for several days, a very high-refueling rate (e.g. 6 channels refueled per day) (Rouben, 2014). Here, 4 channels are refueled per day with an 8-bundle-shift scheme, where 8 high burnup bundles (near the outlet end) are discharged and 4 low burnup bundles (previously near the inlet end) are displaced towards the outlet end by inserting 8 fresh fuel bundles. This scheme is an excellent compromise between increasing the bundle discharge burnup and reducing the channel-visit rate (Rouben, 1997). Bundles moved from low to high-power locations may suffer a cladding rupture leading to undesirable fission products release; such movement should be tested with ATF cladding concepts before implementation.

First, the turn-point day t_p for which every system becomes subcritical is determined. Secondly, refueling is started 10 FPD before the reactor reaches t_p. This time gap avoids a high refueling rate in the first few days and avoids suddenly draining the LZC compartments or removing too rapidly the boron from the moderator. The CANDU's operating license limits are then fully satisfied. The fueling pattern (Fig. 6) is subsequently executed and refueling operations are carried out daily. The reactor has operated for a total of 300FPD (including the period before refueling). Table 5 lists the refueling results during one complete operation cycle, with $N_{chan}^{refueled}$ the number of fuel channels refueled. Fig. 16 shows the core reactivity evolution from the fueling point until 300FPD. Due to the core reactivity around 135 FPD (see Table 3), the refueling of SiC, (FeCrAl, APMT, 304SS) and 310SS cladded-systems start, respectively, 8, 10 and 12 days after the scheduled date for refueling the current CANDU-6 reactor. All systems respond in the same way and 3 main periods can be distinguished. The first period corresponds to a reactivity decline during which the new fuel bundles loaded are not able to counterbalance the burnup effect. The insertion of these bundles just slows down the rate at which k_{eff} decreases. This period lasts 32 days for Zircaloy-II versus 26 days for silicon carbide, and 6 days for both nickel and aluminium systems. The time observed for Zircaloy is the typical delay for the

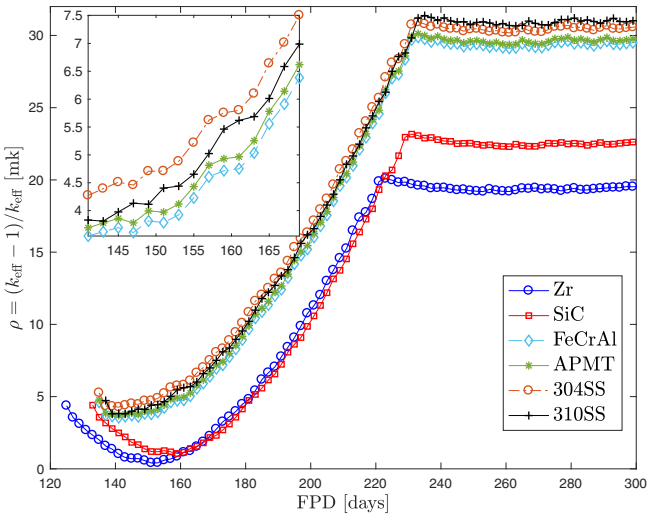

Fig. 16. Reactivity vs. full-power days after refueling operations start.

plutonium peak appearance. We conclude that 1% of ^{235}U enrichment makes it possible to shorten this period from more than one month to less than one week. During the second period, the effect of fresh bundles outweighs the total spent fuel burnup effect. Reactivity increases day by day due to continuous refueling of depleted fuel. Silicon carbide and Zicaloy-II adopt a very similar behavior during this period (only 0.58 mk difference). This period is longer for enriched cores and provides an additional reactivity of 5 mk, on average, when compared to cores cladded with Class I materials. The last period, corresponding to the time averaged core behavior, then sets in during which k_{eff} keeps a relatively constant value. The local fluctuations are due to the discrete nature of CANDU refueling. The first two periods are called transitional or pre-equilibrium conditions (Rouben, 1997), while the third is assimilated with the CANDU equilibrium core. Despite the local ripples, the global core-average characteristics (e.g. channel power distribution and average bundle burnup distribution) have reached steady state, the discharged bundle burnup and the boron concentration are essentially constant.

If the refueling operations are not interrupted, the systems based on silicon carbide, aluminium and nickel alloys continue to operate, respectively, with 5 mk, 10 mk and 11 mk more reactivity than the current CANDU-6 reactor. These reactivities can be decreased if a refueling rate lower than that of Zircaloy is adopted. During the same refueling period, the core with the most transparent sheath (SiC) operates without enrichment with a saving of 256 fresh bundles over a period of 300FPD (see Table 5). The highest fuel economy is then observed in silicon carbide system.

3.6. Loss of regulation control event

The overall CANDU safety takes advantage of its favorable inherent characteristics (e.g. small reactivity coefficients, small

Table 5
Refueling details for one-cycle CANDU-6 operation.

	Zr	SiC	FeCrAl	APMT	310SS	304SS
Turn point (t_p) [days]	136	144	146	146	148	146
$k_{eff}^{non-refueled}(t_p)$	0.99987	0.99984	0.99957	0.99970	0.99969	0.99975
$k_{eff}^{non-refueled}(t_p - 1)$	1.00029	1.00027	1.00003	1.00017	1.00016	1.00022
Fueling point (t_f) [days]	126	134	136	136	138	136
$k_{eff}^{refueled}(t_p)$	1.00158	1.00184	1.00362	1.00379	1.00413	1.00448
$N_{chan}^{refueled}$	380 + 312	380 + 280	380 + 272	380 + 272	380 + 264	380 + 272

change in core global and local parameters, very long prompt neutron lifetime) and its two independent highly reliable shutdown systems (Ovanes et al., 2011; Kastanya et al., 2013). CANDU's defense-in-depth approach has been introduced by the Canadian Nuclear Safety Commission (CNSC) and "*One of the most important aspects of a defense-in-depth philosophy is the prevention of upset conditions and accidents which threaten the integrity of the fuel sheath and the primary coolant system pressure boundary*" (Hurst and Boyd, 1972). Reactivity insertion events are part of the design basis and are cited in the CNSC's latest requirement (RD-337) as: "*The maximum degree of positive reactivity and its maximum rate of increase by insertion in normal operations, AOO [anticipated operational occurrences], and DBAs [design basis accidents] so that no resultant failure of the reactor pressure boundary will occur, cooling capability will be maintained, and no significant damage will occur to the reactor core.*" (Canadian Nuclear Safety Commission, 2014). Here, a normal operation is assumed for one hour, when suddenly all RRS devices malfunction simultaneously in the same direction at their maximum speeds. The core behavior in the hours following the accident is presented in Fig. 17. $\rho(h)$ is the core dynamic reactivity and is computed every hour h as:

$$\rho(h) = \left[\frac{1}{k_{\text{eff,ref}}(h)} - \frac{1}{k_{\text{eff,per}}(h)}\right] \times 1000 \text{ [mk]}. \quad (3)$$

with $k_{\text{eff,ref}}$ and $k_{\text{eff,per}}$ respectively the normal and the perturbed effective multiplication factor. The effect of ADJs and LZCs simultaneous loss is the same for all systems. Cores sheathed with Class I materials record the highest reactivity values. Zircaloy-II and SiC responses differ only by 0.04 mk along the entire transitional period. FeCrAl, APMT, 304SS and 310SS responses are, respectively, 2.8 mk, 2.9 mk, 3.2 mk and 3.5 mk lower than Zircaloy-II. 310SS response is lower than that of 304SS due to the fact that the first contains 11% more ^{59}Ni (Table 1) which has a thermal capture cross section of the order of 600 barns. APMT and FeCrAl have a very similar profile (0.08 mk of differences) due to their equivalent content in ^{56}Fe (Table 1) which has a thermal capture cross section of the order of 10 barns. The drop in reactivity observed in the first 7 h is due to ^{135}Xe increase, resulting from the beta decay of ^{135}I (half-life of 6.585 h). The same accident was simulated at 20 FPD. It was found that the reactivity of Class I systems increases monotonically during the transient due to the ^{239}Pu contribution, while that of Class II decreases constantly as a result of ^{235}U consumption. Two scenarios of return to the nominal conditions are thereafter simulated. In the first (Fig. 18, *left*), it is assumed that the event lasts 8 h after which the plant operator manages to concurrently unlock all regulation mechanisms. In the second (Fig. 18, *right*), we consider a gradual return to normal conditions after 6 h of RRS devices loss; the operator succeeds, hourly, to fill only 5% of the 14 LZCs compartments and to insert only 5% of the 21 ADJs. We conclude that all the systems respond in a very similar way to the current CANDU-6 reactor, for the instantaneous or gradual recovery of the RRS devices.

3.7. Reactivity perturbations

Preventing unacceptable reactivity transients is the first fundamental safety objective in the IAEA (International Atomic Energy Agency) perspective (IAEA, 2000; IAEA, 2005). On-power refueling ensures a stable equilibrium core over the life operation; core global and local parameters are constant with time (Garland, 2014) and both fuel and coolant neutronic properties show an overall axial symmetry (Kastanya et al., 2013). This minimizes ADJ insertion and ejection maneuvers and leaves the LZC compartment fills in the desired operational range around 50% (Rouben, 2014). CANDU thermophysical properties cannot in any case result in a loss of a regulation event because all RRS and ESS devices pass through the moderator (which is maintained at a low temperature and quasi-atmospheric pressure) without penetrating the pressure tubes. Due to the large core size (7.6 m×6 m), any device adverse movement will lead to a reactivity worth of 2.5 mk, far below the total delayed neutron contribution (5.5 mk). Due to the heavy water moderator and its mechanical separation from the fuel bun-

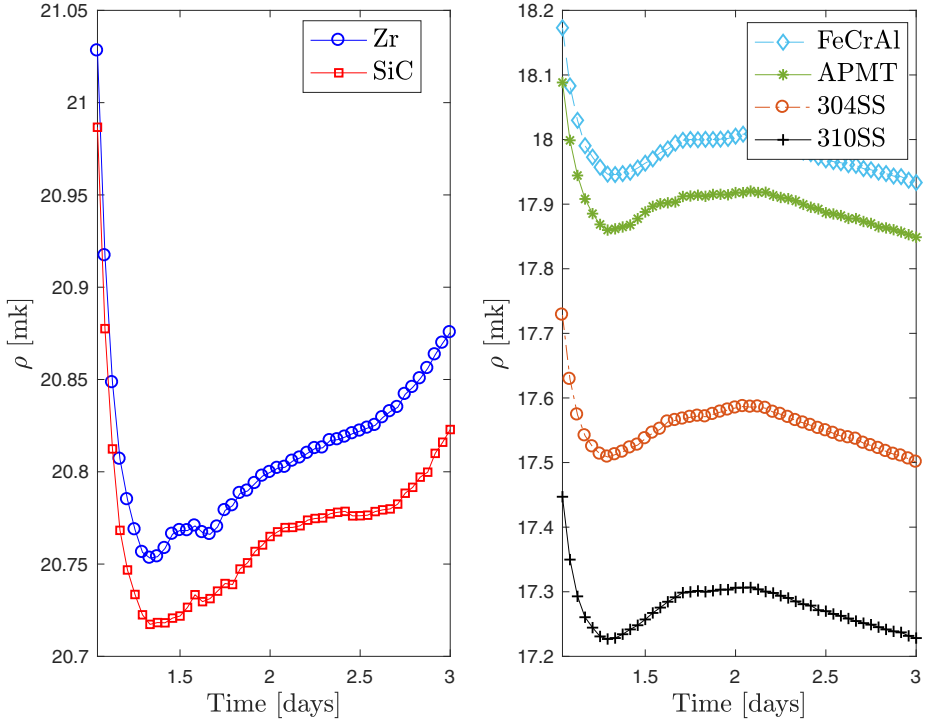

Fig. 17. Reactivity evolution after a loss of regulation control event initiated on day 1.

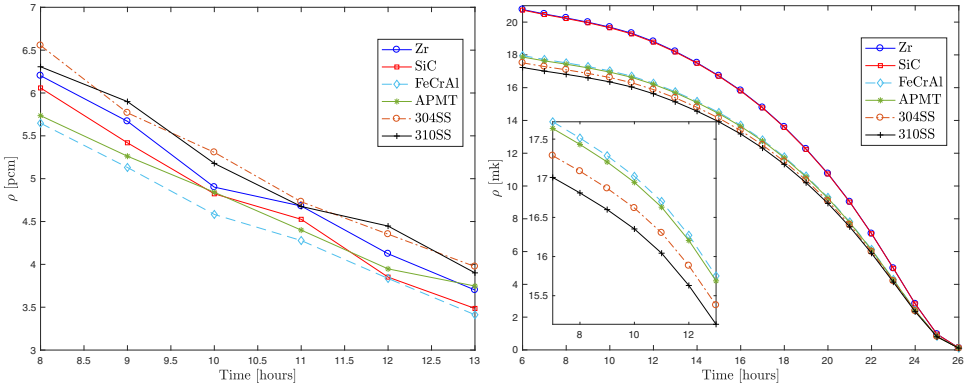

Fig. 18. Reactivity evolution in the case of instantaneous recovery after 8 h (*left*) and progressive recovery (*right*) of RRS devices.

dles, neutron lifetime is 30–45 times longer than that of typical PWRs (Kastanya et al., 2013). This results in a longer reactor period, a lower flux sensitivity to sudden reactivity perturbations and a higher degree of mitigation in reactivity initiated accidents (RIAs). It is not known yet how the CANDU-6 core would react to temperature and density perturbations when cladded with the candidates' materials. Here, the core responses are compared when the following perturbation scenarios are separately examined:

1. coolant temperature (T_c) perturbations are progressively introduced by steps of ±5 K (reference coolant temperature is 560.66 K).
2. moderator temperature (T_m) perturbations are progressively introduced by steps of ±5 K (reference moderator temperature is 345.66 K).
3. fuel temperature (T_f) perturbations are progressively introduced by steps of ± 10 K (reference fuel temperature is 941.29 K).
4. void is progressively accumulated in the coolant volumetric mass density (ρ_v^c) by steps of 2.5% (reference coolant density is 0.8121 g/cm^3).
5. void is progressively accumulated in the moderator volumetric mass density (ρ_v^c) by steps of 2.5% (reference moderator density is 1.0829 g/cm^3).

At every time steps, the core dynamic reactivity is computed as shown in Eq. 3. Fuel is burned under CANDU nominal conditions. Perturbations are introduced uniformly in each cell and applied separately at each burnup steps.

3.7.1. Coolant temperature perturbations

Fig. 19 shows the cores' responses when the coolant temperature is perturbed. As T_c is increased, the neutron thermal equilibrium moves towards higher energies. As a result, the slope of the $\rho(T_c)$ curve is negative at BOC since the fuel then contains only ^{235}U (no plutonium) which has a $1/\sqrt{E}$ fission cross section. For

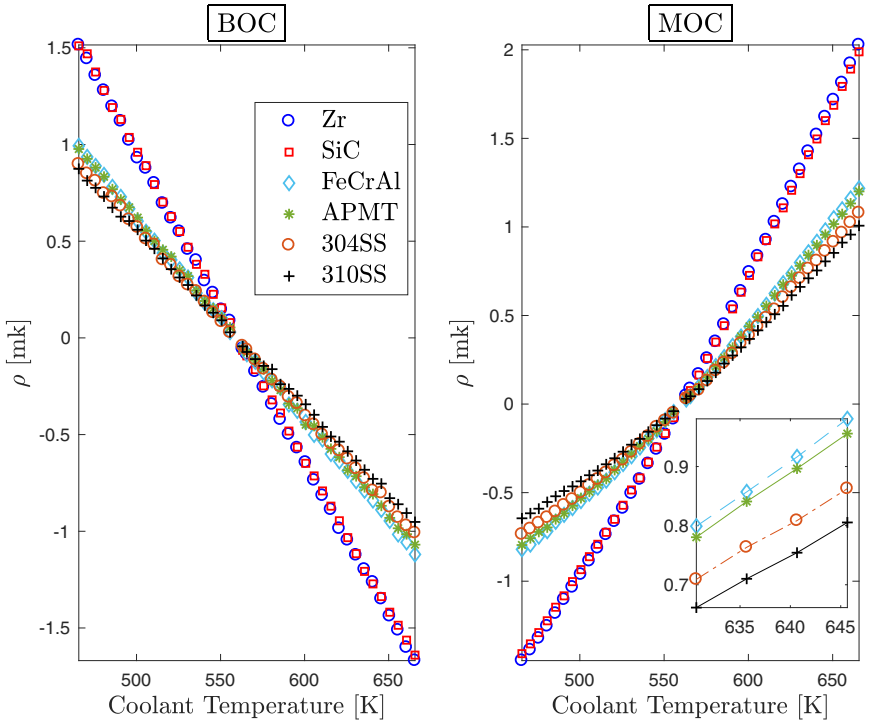

Fig. 19. Coolant temperature perturbations.

Zr and SiC cladding, the slope of the $\rho(T_c)$ curve is somewhat more negative than for Class II claddings. This is mainly due to a slightly faster neutron flux observed for the later claddings. At MOC, the slope of the $\rho(T_c)$ curve is positive due to the presence of ^{239}Pu and ^{241}Pu that have large fission resonances at 0.295 eV. The fact that the slope of the $\rho(T_c)$ curve is somewhat more positive for Zr and SiC cladding is in this case a combination of two effects. A slightly faster neutron flux observed for the Class II claddings and a higher fuel enrichment (slightly larger negative contribution to reactivity from ^{235}U when compared with the positive contribution from plutonium).

3.7.2. Moderator temperature perturbations

Fig. 20 shows that perturbing the moderator temperature results in the same global effect as the coolant temperature perturbation. The main difference is that reactivity values are more than twice as large at BOC, while being 3.5 times higher at MOC. This behavior can be explained in a way similar to that presented in Section 3.7.1, namely an increase in the temperature of the moderator displaces the thermal part of the neutron flux spectrum towards higher energies. As a result, thermal equilibrium with the higher temperature coolant is more easily reached leading to thermal fission in uranium being reduced at BOC while at MOC the presence of plutonium leads to an increase in reactivity. Because the ratio of moderator to coolant volume is 20.75, for the same perturbation ($\Delta T_m = \Delta T_c$), a higher effective neutron temperature is reached leading to a higher fraction of the equilibrium flux overlapping with the plutonium resonance (Whitlock, 1995). Class I and II maximum reactivity differences are below 1.2 mk at BOC. At MOC, Zircaloy cladded fuels have respectively 2.72 mk and 2.99 mk higher reactivities than aluminium and nickel-cladded cores while for SiC the difference with respect to Zircaloy cladded fuel stays below 0.08 mk.

3.7.3. Fuel temperature perturbations

Fig. 21, *left*, shows that increasing the fuel temperature at BOC leads to negative reactivity feedback for both Class I and II-cladded systems. These responses are caused by the Doppler broadening of the low-lying s-wave resonances of ^{238}U. This effect is slightly less pronounced for Class II cladding because of the enriched fuel they contain (less ^{238}U means a larger resonance escape probability). Fig. 21, *right*, shows that increasing T_f at MOC implies a slow positive reactivity increase in Zircaloy and silicon carbide systems, while a net negative reactivity decrease is observed in aluminium and nickel-based systems. This behavior arises from two combined effects. The neutron spectrum is also slightly harder when T_f is increased. Fission also increases due to Doppler broadening of ^{239}Pu thermal resonance which gives a larger negative contribution to ρ than the reduction in resonance escape probability for Class I cladding. This effect is slightly reduced for the Class II claddings that contain enriched fuels (see Naceur and Marleau, 2018 for plutonium inventories as a function of time for the different fuels considered here).

3.7.4. Coolant density perturbations

Analysis of coolant partial or complete voiding and its impact on neutron population is central to the design and the safety systems licensing for CANDU reactors. There is a strong incentive to reduce CANDU's positive reactivity response linking prompt power change and coolant loss (Whitlock, 1995; Talebi et al., 2006; Farkas, 2014). Fig. 22 shows that a monotonic positive reactivity feedback is observed in all cores, with a slight upwards slope when the coolant voiding percentage increases. The fuel bundles are the main fast neutron sources, while the bulk heavy water moderator is a well-thermalized neutron source. Contributing around 0.03% of the overall bundle absorption (Whitlock et al., 1995), the major role of the hot coolant is to slow down fast and high energy epithermal neutrons, and increase the average energy of thermal

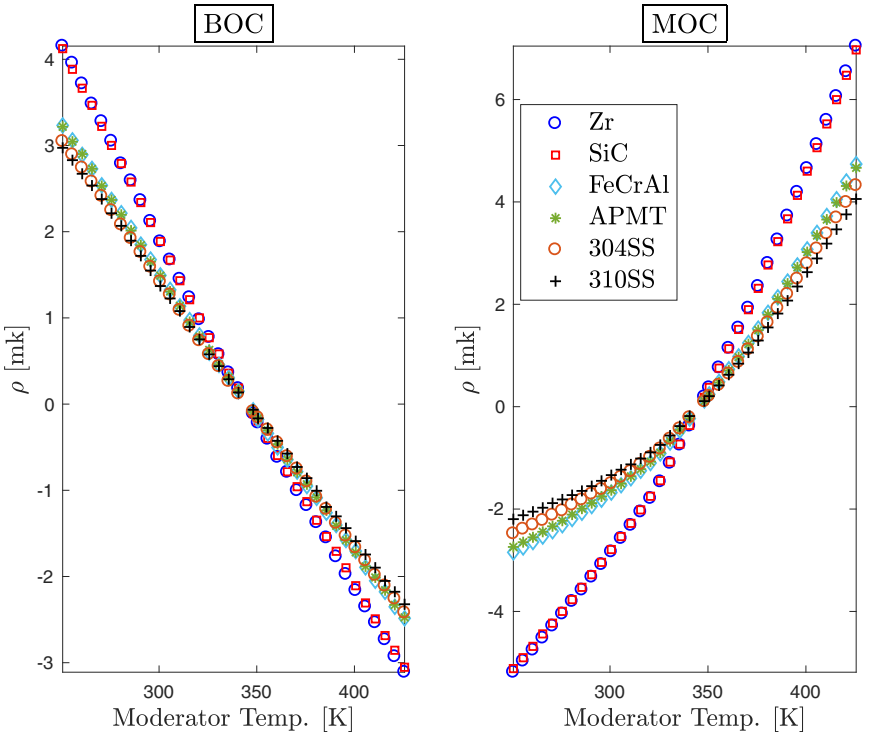

Fig. 20. Moderator temperature perturbations.

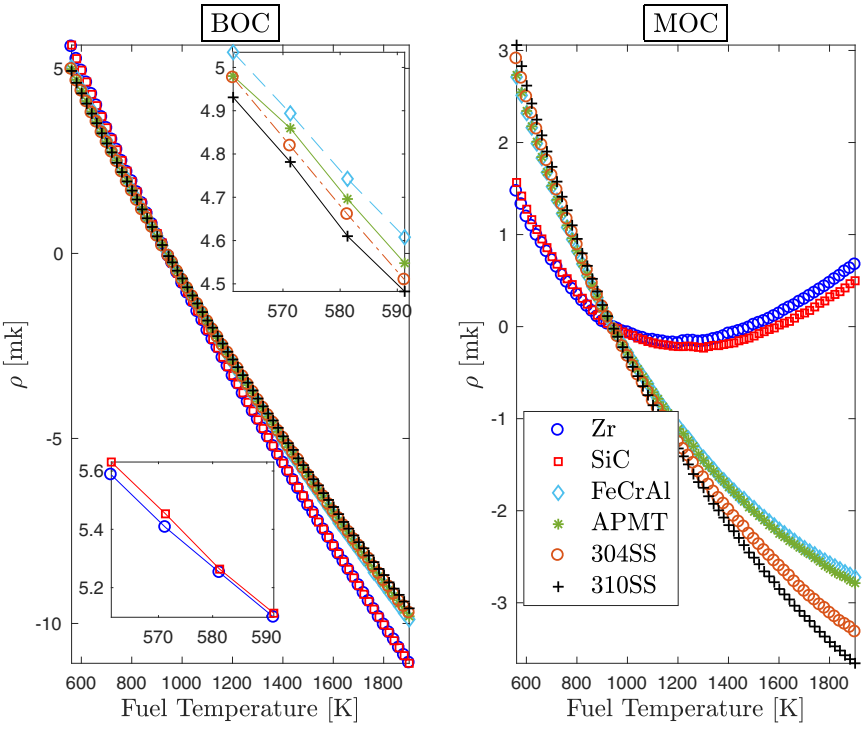

Fig. 21. Fuel temperature perturbations.

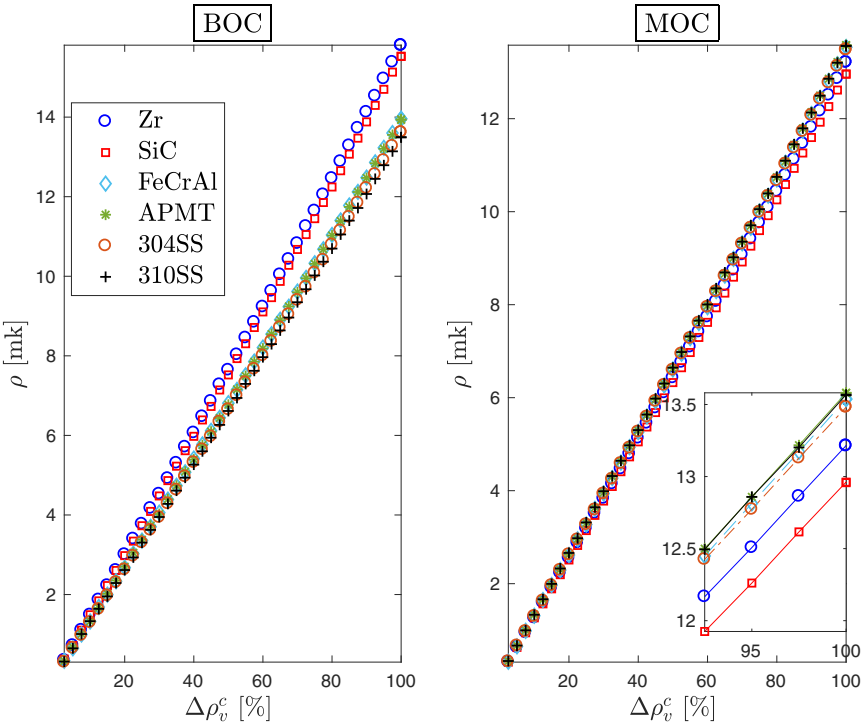

Fig. 22. Coolant volumetric density perturbations.

neutrons. Whitlock (1995) showed that the loss of coolant simultaneously increases ^{238}U parasitic captures and all fissile isotopes fast fission. This spectral shift contributes +2 mk in the equilibrium voided bundle. Assuming a very small coolant contribution to the moderating power ($\gamma\Sigma_s$), loss of coolant also decreases the epithermal flux in all resonances. As a consequence, the resonance escape probability given by

$$p \simeq \exp\left[-\frac{1}{\gamma\Sigma_s}\int \Sigma_c(E)\phi(E)\mathrm{d}E\right]$$

with $\Sigma_c(E)$ being the resonant capture cross-section, decreases. This spectral shift contributes +10.9 mk in the voiding effect at MOC. Reduction in coolant up-scattering shifts the thermal flux towards the moderator low equilibrium temperature. Both the thermal

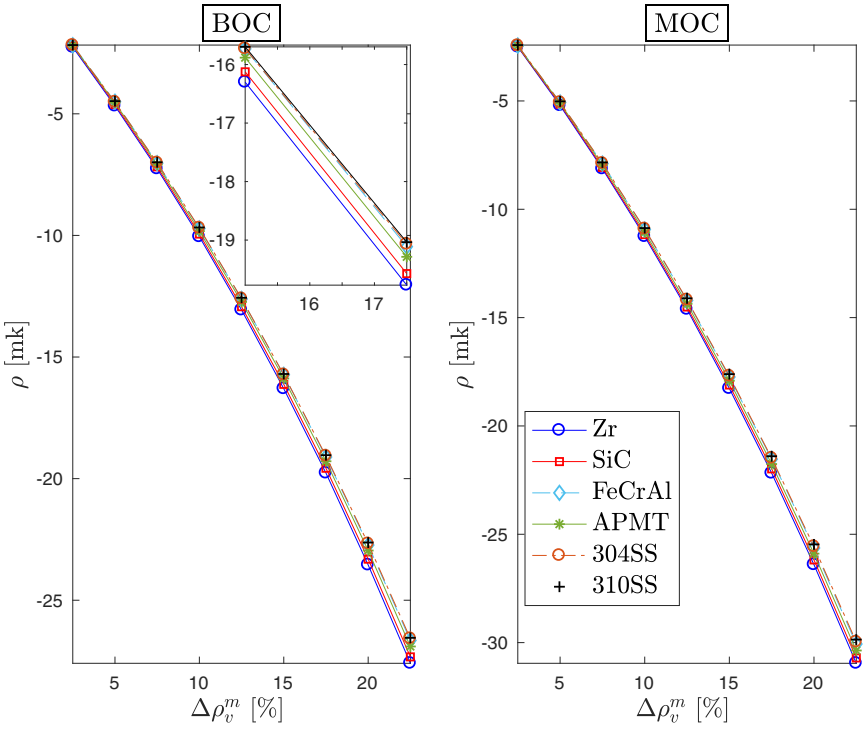

Fig. 23. Moderator volumetric density perturbations.

utilization factor f and thermal fission yield η increase for ^{235}U and decrease for plutonium. This effect is worth + 5.1 mk at zero burnup and close to zero at mid-burnup. This explains the lower void coefficient recorded at MOC (Fig. 22, *right*). At BOC, the higher coolant void reactivity (CVR) is found in Zicaloy and silicon carbide systems (respectively 15.81 mk and 15.52 mk), followed by FeCrAl and APMT (13.96 mk and 13.93 mk) and finally 304SS and 310SS (13.62 mk and 13.50 mk). The lower aluminium and nickel-cladded systems CVR magnitude are due to the cladding thermal and epithermal captures. A higher decrease in CVR with burnup is observed in Class I claddings because of their higher relative plutonium contents.

3.7.5. Moderator density perturbations

Fig. 23 shows that for all cores, a highly negative response to moderator voiding is observed. As the moderator void is increased, the thermalization process is less and less efficient and thermal fission is reduced. This effect is nearly independent of the cladding type.

4. Conclusion

The 2D and 3D DRAGON-DONJON capabilities are exploited to simulate CANDU-6 core operations with accident tolerant claddings under normal and accidental conditions. Core follow-up simulations to 300 full-power days (FPD) of operation are carried out using a 37-element bundle cladded with aluminium-based alloys (FeCrAl and APMT), nickel-based alloys (304SS and 310SS), silicon carbide (SiC) and Zircaloy (Zr-II). High thermal-to-epithermal ^{59}Ni and ^{56}Fe neutronic captures found in nickel and aluminium-cladded bundles are compensated using ^{235}U enrichment to reach the current CANDU-6 bundle cycle-averaged multiplication factor. A 25.1 mk higher core reactivity is observed in aluminium and nickel systems at BOC. Aluminium and nickel-based systems core reactivities dominate the CANDU reference value up to the 235th and 250th FPD, respectively. Enrichment eliminates ^{239}Pu peak in k_{eff} patterns, leading to a lower breeding ratio and a faster core reactivity decline. The most transparent SiC cladding permits CANDU operation with natural uranium, produces a 3.34 mk higher ^{239}Pu peak and a positive $\Delta\bar{k}_{\text{eff}}$ from Zircaloy-II during the complete operation cycle.

To compensate the fresh cores excess reactivity, several iterations were needed in DRAGON-DONJON calculations chain to reach a 0.01 mk convergence criterion. Only 0.1 ppm larger boron concentration from the actual CANDU-6 conditions is needed for the SiC system. The boron concentration increase is found 11 to 13 times higher in aluminium and nickel systems, respectively. Analyzing the power and flux distributions, it is shown that the bundle and channel axial and radial profiles are similar to the expected CANDU's distributions. The channels and bundles with the highest and lowest powers are found exactly in the same locations for all cores. Also, the adjusters and the liquid-zone controllers flux flattening capabilities remain the same for all systems. All systems operations are found in compliance with CANDU operating license limits. A flux hardening is observed in every bundle-cladded with aluminum or nickel-based alloys. Despite the higher enrichment, 310SS, 304SS, APMT and FeCrAl systems, show, respectively, 19.81%, 18.31%, 16.52% and 16.06% lower thermal flux than the CANDU reference system. SiC and Zircaloy flux differences are below 0.3%. The flux hardening effect results in a 245.8 kW lower channel power in nickel and aluminium-based systems. For nickel-based claddings, the time-averaged maximum channel and bundle power penalties from-Zircaloy are respectively around 106.4 kW and 22.6 kW. Zircaloy maximum channel power exceeds the silicon carbide system only by 1.45 kW. To compensate the fuel burnup, an 8-bundle shift on-power refueling scheme based on the CANDU channel age model is tested. SiC, (FeCrAl, APMT, 304SS) and 310SS-cladded systems' refueling operations start, respectively, 8, 10 and 12 days after the CANDU-6 scheduled refueling date. An equilibrium core state is reached in all systems. Silicon carbide, aluminium and nickel-based cores continue respectively to operate with 5 mk, 10 mk and 11 mk excess in reactivity

compared to Zircaloy system. The highest fuel economy is observed in silicon carbide system with a saving of 256 fresh bundles, compared to Zircaloy-II, over a period of 300FPD.

A complete loss of regulation control event was also simulated. Zr and SiC responses differ only by 0.04 mk. Aluminium and nickel-cladded systems' responses are, respectively, 2.8 mk and 3.5 mk lower than the current CANDU response. All systems respond in a similar way to the instantaneous or gradual recovery of reactor regulating devices. By uniformly perturbing the core global and local parameters, moderate and severe DB accident scenarios are simulated. Due to ^{239,241}Pu absence at BOC, the coolant and the moderator temperature coefficients are respectively 1.0 mk and 2.72 mk lower in aluminium and nickel systems. At MOC, the Doppler effect is found negative in enriched cores, while positive in Zircaloy and silicon carbide systems. The CVR magnitude is reduced by 1.88 mk and 2.31 mk in aluminium and nickel systems, respectively.

Based on this methodology, we will next quantify the neutronic advantages and penalties when chromia, alumina and silica materials are used in a CANFLEX® bundle and as structural components in the Canadian-SCWR (supercritical water reactor). For CANDU, particular focus should now be placed on experimental and prototypical testing environments for these materials.

Acknowledgments

The authors acknowledge the Natural Sciences and Engineering Research of Canada (NSERC) for partly funding this work. One of the authors (AN) wishes to thank Yasamin Majedi for her valuable help in grammar and speller checking.

References

Ambartsumyan, R., Kiselev, A., et al., 1959. Mechanical properties and corrosion resistance of zirconium and its alloys in water, steam and gases at elevated temperatures. Tech. rep., USSR/A/CONF.15/P/2044.

Ang, C., Raiman, S., Burns, J., Hu, X., Katoh, Y., 2017. Evaluation of the First Generation Dual-purpose Coatings for SiC Cladding. Tech. rep., ORNL, SR-2018/318.

Atomic Energy of Canada Limited, 2005. CANDU-6 Technical Summary. Mississauga, ON, Canada.

Bieman, D., Bird, P., 1992. The Moderator Liquid Poison System. Reactor & Auxiliaries. Course 233. Module 4. Nuclear Training Center, Chalk River, ON, Canada.

Brachet, J., Le Saux, M., Le Flem, M., Urvoy, S., Rouesne, E., Guilbert, T., Cobac, C., Lahogue, F., Rousselot, J., Tupin, M., et al., 2015. On-going studies at CEA on chromium coated zirconium based nuclear fuel claddings for enhanced accident tolerant LWRs fuel. In: Top Fuel 2015, September 13–17. Zurich, Switzerland, pp. 13–19.

Brassfield, H., White, J., Sjodahl, L., Bittel, J., 1968. Recommended Property and Reactions Kinetics Data For Use in Evaluating a Light-Water-Cooled Reactor Loss-of-Coolant Incident Involving Zircaloy-4 Or 304SS Clad UO2. Tech. rep., General Electric Co., Cincinnati, OH (United States). Missile and Space Division, GEMP-482.

Burns, P., Ewing, R., Navrotsky, A., et al., 2012. Nuclear fuel in a reactor accident. Science (Washington) 335 (6073), 1184–1188.

Canadian Nuclear Safety Commission, 2014. RD-337: Design of New Nuclear Power Plants.https://goo.gl/joq1kh, online; (accessed 5 February 2018).

Carruthers, E., Chow, H., 1997. Simulations of Darlington FINCH Refuelling Transient. In: Proceedings of the Eighteenth Annual Conference of the Canadian Nuclear Society, June 8–11. Toronto, Canada.

Chaplin, R., 2014. The Essential CANDU, A Textbook on the CANDU Nuclear Power Plant Technology, Ch. Genealogy of CANDU Reactors. In: garland2014essential.

Cheng, H., 1980. Review of light water reactor safety. In: Joint nuclear power and technology conference, Decembre 14–21, 1980. Taipei, Taiwan.

Corey, G., 1979. A brief review of the accident at Three Mile Island. IAEA Bull. 21 (5), 54–59.

D'Antonio, M., Donnelly, J., 1997. Explicit Core-Follow Simulations for a CANDU 6 Reactor Fuelled with Recovered-Uranium CANFLEX Bundles. In: Proceedings of the Fifth International CNS CANDU Fuel Conference, September 21–25. Toronto, ON, Canada, pp. 82–90.

Donnelly, J., 1986. WIMS-CRNL: a user's manual for the Chalk River version of WIMS. Tech. Rep. AECL-8955, Canada.

Farkas, R., 2014. Moderator displacers for reducing coolant void reactivity in CANDU reactors: a neutronics scoping study. Institute of Technology, University of Ontario, Canada (Master's thesis).

Garland, W. (Ed.), 2014. The Essential CANDU, A Textbook on the CANDU Nuclear Power Plant Technology. University Network of Excellence in Nuclear Engineering (UNENE), Hamilton, ON, Canada.

George, N.M., Terrani, K., Powers, J., Worrall, A., Maldonado, I., 2015. Neutronic analysis of candidate accident-tolerant cladding concepts in pressurized water reactors. Ann. Nucl. Energy 75, 703–712.

Glasstone, S., Sesonske, A., 2012. Nuclear Reactor Engineering: Reactor Systems Engineering. Springer Science & Business Media, New York, NY, USA.

Goldman, K., 1953. Report of the March 1953 Meeting of the Zirconium Alloy Corrosion Committee. Tech. rep., Westinghouse Electric Corp. Atomic Power Div., Pittsburgh.

Goldner, F., 2012. Development strategy for advanced LWR fuels with enhanced accident tolerance. Tech. rep., US.DOE Office of Nuclear Energy (NE), DOE/NE-061212-NEAC-Goldner.

Hébert, A., 1987. Development of the nodal collocation method for solving the neutron diffusion equation. Ann. Nucl. Energy 14 (10), 527–541.

Hébert, A., 2016. Applied Reactor Physics. Presses Inter, Polytechnique, Montreal, QC, Canada.

Hébert, A., 2017. A User Guide for TRIVAC Version4. Institut de génie nucléaire, Département de génie mécanique, École Polytechnique de Montréal. Montréal, QC, Canada, Tech. Rep. IGE-293.

Hébert, A., Marleau, G., 1991. Generalization of the Stamm'ler method for the self-shielding of resonant isotopes in arbitrary geometries. Nucl. Sci. Eng. 108 (3), 230–239.

Hébert, A., Sekki, D., Chambon, R., 2018. A User Guide for DONJON Version5. Institut de génie nucléaire, Département de génie mécanique, École Polytechnique de Montréal. Montréal, QC, Canada, Tech. Rep. IGE-344.

Hellström, K., Israelsson, N., Mortazavi, N., Canovic, S., Halvarsson, M., Svensson, J.-E., Johansson, L.-G., 2015. Oxidation of a dispersion-strengthened powder metallurgical FeCrAl alloy in the presence of O2 at 1100 °C: the influence of water vapour. Oxid. Met. 83 (5–6), 533–558.

Hurst, D., 1997. Canada Enters the Nuclear Age: A Technical History of Atomic Energy of Canada Limited as Seen From its Research Laboratories. McGill-Queen's University Press.

Hurst, D., Boyd, F., 1972. Reactor licensing and safety requirements. Can. Nucl. Assoc. 18, 195.

IAEA, 1993. Fuel Failure in Normal Operation of Water Reactors: Experience, Mechanisms and Management. Tech. rep., IAEA, Vienna, IAEA-TECDOC-709.

IAEA, 2000. Safety of Nuclear Power Plants: Design, Safety Standards Series No. NS-R-1, IAEA, Vienna. Tech. rep., IAEA, Vienna, IAEAL 12-00719.

IAEA, 2005. Assessment of Defence in Depth for Nuclear Power Plants, Safety Reports Series No.46, IAEA, Vienna. Tech. rep., IAEA, Vienna, IAEAL 04-00388.

IAEA, 2015. The Fukushima Daiichi Accident: Description and Context of the Accident. Tech. rep., Technical Volume 1/5: Description and Context of the Accident, IAEAL 15-00988.

Ishibashi, R., Tanabe, S., Kondo, T., Yamashita, S., Nagase, F., 2017. Improving the corrosion resistance of silicon carbide for fuel in BWR environments by using a metal coating. In: Water Reactor Fuel Performance Meeting (WRFPM 2017), September 10-14. Jeju, Korea.

Ishida, T., Harayama, Y., Yaguchi, S., 1986. Oxidation of 304 stainless steel in high-temperature steam. J. Nucl. Mater. 140 (1), 74–84.

Johnston, W., 1977. Three years after the hearings. In: Zirconium in the Nuclear Industry. ASTM International, West Conshohocken, PA, USA.

Karoutas, Z., Brown, J., Atwood, A., Hallstadius, L., Lahoda, E., Ray, S., Bradfute, J., 2018. The maturing of nuclear fuel: past to Accident Tolerant Fuel. Prog. Nucl. Energy 102, 68–78.

Kass, S., 1954. Report of October 1954 Meeting of the Zirconium Alloy Corrosion Committee. Tech. rep., Westinghouse Electric Corp. Atomic Power Div., Pittsburgh, WAPD-MM-713.

Kastanya, D., Boyle, S., Hopwood, J., Park, J.H., 2013. The impact of power coefficient of reactivity on CANDU-6 reactors. Nucl. Eng. Technol. 45 (5), 573–580.

Kaufmann, A., 1948. Technical Progress Report For the Period February Through April 1948 At MIT. Tech. rep., Massachusetts Inst. of Tech., Cambridge. Metallurgical Group, MIT-1004.

Koning, A., Forrest, R., Kellett, M., Mills, R., Henriksson, H., Rugama, Y., et al., 2006. The JEFF-3.1 nuclear data library. OECD, Paris, France.

Koo, Y., Yang, J., Park, J., Kim, K., Kim, H., Kim, D., Jung, Y., Song, K., 2014. KAERI's development of LWR accident-tolerant fuel. Nucl. Technol. 186 (2), 295–304.

Lewis, W., 1956. The Canadian research reactors and their uses. Br. J. Appl. Phys. 7 (S5), S96.

Lustman, B., Kerze, F., 1955. The metallurgy of zirconium, vol. 4. McGraw-Hill Book Company, Belmont, Massachusetts, USA.

Luxat, J.C., 2009. Thermal-Hydraulic aspects of progression to severe accidents in CANDU reactors. Nucl. Technol. 167 (1), 187–210.

Marleau, G., Hébert, A., Roy, R., 1992. New computational methods used in the lattice code DRAGON. In: Topical Meeting on Advances in Reactor Physics, March 8-11. Vol. 1. Charleston Sheraton, Charleston, SC, USA, pp. 8–11.

Marleau, G., Hébert, A., Roy, R., 2018. A User Guide for DRAGON Version 5. Institut de génie nucléaire, Département de génie physique, École Polytechnique de Montréal. Montréal, QC, Canada, Tech. Rep. IGE-335.

Merckx, K., 1958. Fuel element design handbook. Tech. rep., General Electric Co., Richland, WA (United States). Hanford Atomic Products Operation. HW-51000-Del, ON: DE95006604, TRN: 95:002746.

Motta, A., Couet, A., Comstock, R., 2015. Corrosion of zirconium alloys used for nuclear fuel cladding. Annu. Rev. Mater. Res. 45 (1), 311–343.

Naceur, A., Marleau, G., 2018. Neutronic analysis for accident tolerant cladding candidates in CANDU-6 reactors. Ann. Nucl. Energy 113, 147–161.
Nuclear Energy Agency, 2012. Nuclear Fuel Safety Criteria: Technical Review. Tech. rep., OECD, NEA, Report No.7072, Second Ed.
Ott, L., Robb, K., Wang, D., 2014. Preliminary assessment of accident-tolerant fuels on LWR performance during normal operation and under DB and BDB accident conditions. J. Nucl. Mater. 448 (1–3), 520–533.
Ovanes, M., Rife, G., Cormier, M., Hopwood, J., 2011. Enhanced CANDU-6: Reactor core safety design. In: Proceedings of International Congress on Advances in Nuclear Power Plants (ICAPP), May 2–6. Nice, France.
Page, R., 1976. Canadian Power Reactor Fuel. Atomic Energy of Canada Limited, Power Projects, Mississauga, ON, Canada.
Pint, B., Terrani, K., Brady, M., Cheng, T., Keiser, J., 2013. High temperature oxidation of fuel cladding candidate materials in steam-hydrogen environments. J. Nucl. Mater. 440 (1–3), 420–427.
Pint, B.A., 2017. Performance of FeCrAl for accident-tolerant fuel cladding in high-temperature steam. Corros. Rev. 35 (3), 167–175.
Pint, B.A., Terrani, K.A., Yamamoto, Y., Snead, L.L., 2015. Material selection for accident tolerant fuel cladding. Metall. Mater. Trans. E 2 (3), 190–196.
Pomerance, H., 1948. Thermal neutron absorption cross sections for separated isotopes. Atomic Energy Commission, Oak Ridge, TN, USA.
Pomerance, H., Oct 1952. Thermal neutron capture cross sections. Phys. Rev. 88, 412–413.
Rae, H., 1997. Canada Enters the Nuclear Age: a technical history of Atomic Energy of Canada Limited as seen from its research laboratories, Ch. CANDU and its Evolution. In: hurst1997canada.
Rebak, R.B., Terrani, K.A., Gassmann, W.P., Williams, J.B., Ledford, K.L., 2017. Improving nuclear power plant safety with FeCrAl alloy fuel cladding. MRS Adv. 2 (21–22), 1217–1224.
Rickover, H., 1975. The Decision to Use Zirconium in Nuclear Reactors. TID-26740. William J. Kroll Medal, Presentation, Denver, Colorado, USA, March 21.
Rogovin, M., 1980. Three Mile Island: A report to the commissioners and to the public. Vol. 2. Nuclear Regulatory Commission, Special Inquiry Group, Rockville, Maryland, USA.
Rouben, B., 1995. Overview of current RFSP-code capabilities for CANDU core analysis. Trans. Am. Nucl. Soc. 72, 339–440.
Rouben, B., 1997. Fuel Management in CANDU. Presentation at Chulalongkorn University Bangkok, Thailand, December 1997.https://bit.ly/2lMe22T, online (accessed 10 January 2018).
Rouben, B., 2002. RFSP-IST, the industry standard tool computer program for CANDU reactor core design and analysis. In: The 13th Pacific Basin Nuclear Conference, October 21–25, 2002. Shenzhen, China.
Rouben, B., 2014. The Essential CANDU, A Textbook on the CANDU Nuclear Power Plant Technology, Ch. CANDU-In-Core Fuel Management. In: garland2014essential.
Roy, R., Marleau, G., Tajmouati, J., Rozon, D., 1994. Modelling of CANDU reactivity control devices with the lattice code DRAGON. Ann. Nucl. Energy 21 (2), 115–132.
Rozon, D., Shen, W., 2001. A parametric study of the DUPIC fuel cycle to reflect pressurized water reactor fuel management strategy. Nucl. Sci. Eng. 138 (1), 1–25.
Sakamoto, K., Hirai, M., Ukai, S., Kimura, A., Yamaji, A., Kusagaya, K., Kondo, T., Yamashita, S., 2017. Overview of japanese development of accident tolerant FeCrAl-ODS fuel claddings for BWRs. In: Water Reactor Fuel Performance Meeting, September 10-14. Jeju Island, Korea.
Sawatzky, A., 1960. The diffusion and solubility of hydrogen in the alpha phase of Zircaloy-2. J. Nucl. Mater. 2 (1), 62–68.
Sawatzky, A., Ells, C., 2000. Understanding hydrogen in zirconium. In: Zirconium in the Nuclear Industry: Twelfth International Symposium, June 15-18. Toronto, ON, Canada.
Sawatzky, A., Ledoux, G., Tough, R., Cann, C., 1982. Hydrogen diffusion in zirconium-niobium alloys. In: Proceedings of the Miami International Symposium on Metal-Hydrogen Systems, April 13–15. Elsevier, Miami Beach, Florida, USA, pp. 109–120.
Shanes, F., Olive, C., Cheng, I., Banica, C., Newman, C., Nainer, O., 2006. Simulation of the Point Lepreau core-follow history with SORO. In: Nuclear energy: a world of service to humanity 27th annual conference of the Canadian Nuclear Society and 30th Canadian Nuclear Society/Canadian Nuclear Association student conference, June. Canadian Nuclear Society, Toronto, Canada, pp. 11–14.
Shen, W., Schwanke, P., 2012. Evolution of RFSP 3.5 for CANDU Analysis. In: Proceedings of the 33rd Annual Canadian Nuclear Society Conference 2012, June 10–13. Saskatoon, Canada.
Snead, M.A., Katoh, Y., Koyanagi, T., Singh, G.P., 2017. SiC/SiC Cladding Materials Properties Handbook. Oak Ridge, TN, USA.
Sowder, A., 2012. International Collaboration for Development of Accident Resistant Light Water Reactor Fuel. In: OECD/NEA Workshop on Accident Tolerant Fuels of LWRs, December 10-12. Issy-les-Moulineaux, France.
St-Aubin, E., 2013. Ajustement du rechargement et des mécanismes de réactivité des réacteurs CANDU pour les cycles de combustible avancés. École Polytechnique de Montréal (Ph.D. thesis).
St-Aubin, E., Marleau, G., 2015. CANDU-6 fuel optimization for advanced cycles. Nucl. Eng. Des. 293, 371–384.
St-Aubin, E., Marleau, G., 2015b. CANDU-6 reactivity devices optimization for advanced fuel cycles – Part I: Adjuster rods optimization. Nucl. Eng. Des.
St-Aubin, E., Marleau, G., 2005. Optimized CANDU-6 cell and reactivity device supercell models for advanced fuels reactor database generation. Ann. Nucl. Energy 85, 331–336.
Steinbrück, M., Vér, N., Groe, M., Oct 2011. Oxidation of Advanced Zirconium Cladding Alloys in Steam at Temperatures in the Range of 600–1200 °C. Oxid. Met. 76 (3), 215–232.
Talebi, F., Marleau, G., Koclas, J., 2006. A model for coolant void reactivity evaluation in assemblies of CANDU cells. Ann. Nucl. Energy 33 (11–12), 975–983.
Terrani, K., 2018. Accident tolerant fuel cladding development: Promise, status, and challenges. J. Nucl. Mater. 501, 13–30.
Terrani, K.A., Pint, B.A., Parish, C.M., Silva, C.M., Snead, L.L., Katoh, Y., 2014. Silicon carbide oxidation in steam up to 2 MPa. J. Am. Ceram. Soc. 97 (8), 2331–2352.
U.S. Atomic Energy Commission, 1973. Acceptance Criteria for Emergency Core Cooling Systems for Light Water Cooled Nuclear Power Reactors. Tech. rep., USAEC RM-50-1.
Uwaba, T., Ito, M., Maeda, K., 2011. Diametral strain of fast reactor MOX fuel pins with austenitic stainless steel cladding irradiated to high burnup. J. Nucl. Mater. 416 (3), 350–357.
Varin, E., Marleau, G., 2006. CANDU reactor core simulations using fully coupled DRAGON and DONJON calculations. Ann. Nucl. Energy 33 (8), 682–691.
Varin, E., Roy, R., Baril, R., Hotte, G., 2004. CANDU-6 operation post-simulations using the reactor physics codes DRAGON/DONJON. Ann. Nucl. Energy 31 (18), 2139–2155.
Whitlock, J., 1995. Reduction of the Coolant Void Reactivity Effect in a CANDU Lattice Cell. McMaster University (Ph.D. thesis).
Whitlock, J., Garland, W., Milgram, M., 1995. Effects contributing to positive coolant void reactivity in CANDU. Trans. Am. Nucl. Soc 72, 329.
Wight, A., Sibley, R., 1977. Fuel Management Design Program. TDAI-105, AECL Power Projects (1977 August).
Woddi, T., Charlton, W., Nelson, P., 2009. India's Nuclear Fuel Cycle: Unraveling the Impact of the U.S.-India Nuclear Accord. In: Synthesis Lectures on Nuclear Technology and Society. Morgan & Claypool Publishers, San Rafael, CA, USA.
Wright, I.G., Barry Dooley, R., 2011. Morphologies of oxide growth and exfoliation in superheater and reheater tubing of steam boiler. Mater. High Temp. 28 (1), 40–57.
Zinkle, S., Terrani, K., Gehin, J.C., Ott, L.J., Snead, L.L., 2014. Accident tolerant fuels for LWRs: a perspective. J. Nucl. Mater. 448 (1), 374–379.